OXFORD

Journal of Petrology, 2024, **65**, egae068
https://doi.org/10.1093/petrology/egae068
ADVANCE ACCESS PUBLICATION DATE 19 JUNE 2024
Original Manuscript

A Geodetically Constrained Petrogenetic Model for Evolved Lavas from the January 1997 Fissure Eruption of Kīlauea Volcano

MELISSA A. SCRUGGS [1,*], FRANK J. SPERA[1], MATT RIOUX[1] and WENDY BOHRSON[2]

[1]Department of Earth Science, University of California Santa Barbara, 1006 Webb Hall, Santa Barbara 93106-9630, CA, USA
[2]Department of Geology and Geological Engineering, Colorado School of Mines, 1516 Illinois Street, Golden 80401, CO, USA

*Corresponding author. E-mail: TheVolcanoDoc@gmail.com

Magmatic systems below volcanoes are often dominated by partially crystalline magma over the long term. Rejuvenation of these systems during eruptive events can impact lava composition and eruption style—sometimes resulting in more violent or explosive activity than would be expected, as was the case at Fissure 17 during Kīlauea's 2018 eruption. Here, we explore how the crystallinity of unerupted intrusion magmas affect hybrid magma compositions and petrological signatures by constructing phase-equilibria models to evaluate mineral and melt compositions of low-MgO lavas erupted along the East Rift Zone of Kīlauea volcano on 30 to 31 January 1997 (Episode 54, Fissures A-F). We then compare calculated mixing proportions and petrologically derived magma volumes to GPS-based geodetic inversions of ground deformation and intrusion growth in an attempt to reconcile geodetic and petrologically estimated magma volumes. Open-system phase-equilibria thermodynamic models were used to constrain the composition, degree of differentiation, and thermodynamic state of a rift-stored, two pyroxene + plagioclase saturated low-MgO magma body immediately preceding its mixing with high-MgO recharge and degassed drainback (lava lake) magma from Pu'u'ō'ō', shortly before fissure activity within Nāpau Crater began on 29 January 1997. Mixing models constructed using the Magma Chamber Simulator reproduce the mineralogy and compositions of Episode 54 lavas within uncertainties and suggest that the identity of the low-MgO magma body may be either variably differentiated remnants of un-erupted magmas intruded into Nāpau Crater in October 1968, or another spatially and compositionally similar magma body. We find that magmas derived from a single, compositionally stratified magma emplaced beneath Nāpau Crater in 1968 can mix with mafic Kīlauea magmas to reproduce average Episode 54 bulk lava, mineralogy and mineral compositions without necessitating the interaction of multiple, low-MgO rift-stored magma bodies to produce Episode 54 lava compositions. Further, by constructing phase equilibria-based mixing models of Episode 54, we can better define the pre-eruptive state of the magmatic system. The resultant mineral assemblages and compositions are consistent with the possibility that the now-fractionated, rift-stored magma body was compositionally stratified and ~40% to 50% crystalline at the time of mixing. Finally, we estimate the volume of the low-MgO magma body to be ~7.51 Mm^3. Phase-equilibria model results corroborate field and geochemical relationships demonstrating how shallow intrusions at intraplate shield volcanoes can crystallize, evolve, and then be remobilized by new, later batches of mafic magma. Most notably, our MCS models demonstrate that the pre-eruptive conditions of an intrusive body may be recovered by examining mineral compositions within mixed lavas. Discrepancies between the geodetic constraints on volumes of stored rift versus newly intruded (recharge) magma and our best-fit results produced by MCS mixing models (which respectively are $m_{mafic}:m_{low\text{-}MgO} \approx 2$ vs. $m_{mafic}:m_{low\text{-}MgO} \approx 0.75$) are interpreted to highlight the complex nature of incomplete mixing on more localized scales as reflected in erupted lavas, compared to geodetically constrained volumes that likely reflect large spatial scale contributions to a magmatic system. These dissimilar volume relationships may also help to constrain eruptive versus unerupted volumes in magmatic systems undergoing mixing. By demonstrating the usefulness of MCS in modeling past eruptions, we highlight the potential to use it as a tool to aid in petrologic monitoring of ongoing activity.

Key words: Magma Mixing; Episode 54; Kīlauea volcano; Magma Chamber Simulator; Geodesy

INTRODUCTION

Nearly continuous eruptive activity at the summit of Kīlauea and along its East Rift Zone (ERZ) has fascinated the public and geoscientists around the world for over four decades. Rapid technological advances of the late 20th and early 21st century—throughout the duration of the 1983–2018 Pu'u'ō'ō'eruption—provided detailed records of the eruption, making Kīlauea one of the best monitored and most intensely studied volcanoes on Earth. This was exemplified from March through April 2018 during the waning stages of the Pu'u'ō'ō'eruption, as Hawaiian Volcano Observatory (HVO) volcanologists were able to accurately forecast the onset of new eruptive activity in the Leilani Estates subdivision in time to avoid loss of life (Neal *et al.*, 2019).

The Pu'u'ō'ō'eruption initiated along the Middle ERZ on 3 January 1983, when a dike from Kīlauea's summit reservoir intruded into a section of the rift zone and encountered a small body of differentiated, rift-stored magma, likely remaining from Kīlauea's 1977 eruption (Garcia *et al.*, 1992, 2000). What followed was a series of almost continuous eruptions that would last over 35 years (Neal *et al.*, 2019). Decade-long periods of passive effusion were routinely punctuated by discrete mixing events, where magmas intruded into the ERZ during the Pu'u'ō'ō'eruption encountered magma in arrested-dike remnants from previous eruptions

RECEIVED JULY 21, 2023; **REVISED** MAY 1, 2024; **ACCEPTED** JUNE 8, 2024

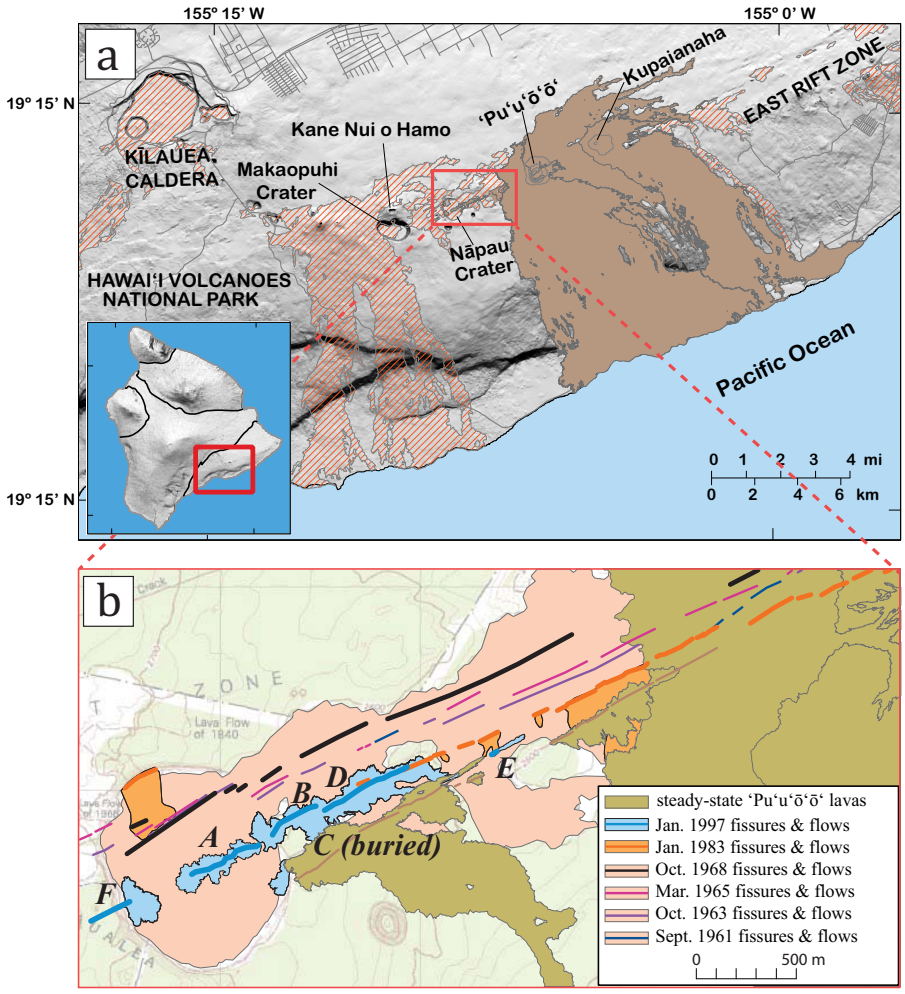

Fig. 1. Map of Kīlauea volcano on the island of Hawai'i (a; after Orr, 2014), and map of fissures within Nāpau Crater (b; modified from Thornber *et al.*, 2015). Steady-state lavas in panel (a) are lavas of the Pu'u'ō'ō'eruption erupted between 1983–2011; those displayed in a hatched pattern are pre-1983 lavas. Note that Pu'u'ō'ō'= Pu'u 'Ō'ō; name updated in 2018 by the Hawai'i Board on Geographic Names to reflect the eruption's end.

(Thornber *et al.*, 2003a; Wright & Klein, 2014; Walker *et al.*, 2019), often resulting in the relocation of vents and/or major reorganization of the underlying magmatic system (Orr, 2014). Here, we use individual mixing events as a petrologic tool to track changes in—and components of—Kīlauea's magma storage and transport system, focusing on a series of fissure eruptions that occurred at the end of January 1997, commonly referred to as Episode 54 (Thornber *et al.*, 1997).

A DETAILED LOOK AT THE EVENTS SURROUNDING EPISODE 54

At 0445 UTC on 30 January 1997 (18:45 HST 29 January 1997), a number of seismic tremor sequences were accompanied by slippage of the south flank decollement and extension across the ERZ in the vicinity of Nāpau Crater (Owen *et al.*, 2000; Segall *et al.*, 2001). Within an hour, 'a loud whooshing roar' (Harris *et al.*, 1997) accompanied ground deflation measured at both Makaopuhi Crater and the Kīlauea summit—consistent with the removal of magma from those sources—and the disappearance of lava from Pu'u'ō'ō'crater (Harris *et al.*, 1997; Owen *et al.*, 2000; Thornber *et al.*, 2003a). Geodetic measurements indicate that rift failure initiated a fracture that rapidly grew, filling with magma from storage reservoirs both up- and down-rift (Owen *et al.*, 2000; Segall *et al.*, 2001; Desmarais & Segall, 2007). This passive intrusion intersected the ground surface at ~1240 UTC (~2:40 a.m. HST, 30 January 1997), initiating Episode 54, a 22-hour-long fissure eruption up-rift of Pu'u'ō'ō', at Nāpau Crater (Fig. 1b). Six eruptive fissures (named Fissures A-F) opened within Nāpau Crater (Fig. 1b) before the eruption ended at 1033 UTC (12:33 a.m. HST, 31 January 1997; Harris *et al.*, 1997). After a 24-day hiatus in activity, a small lava pond appeared within Pu'u'ō'ō', signaling that Kīlauea's plumbing system was beginning to recover, and marking the start of Episode 55 (Harris *et al.*, 1997; Owen *et al.*, 2000; Thornber *et al.*, 2003a). The lava lake refilled for a period of 32 days, and sporadic outbreaks of lava from the flanks of Pu'u'ō'ō'began on 28 March 1997 (Garcia *et al.*, 2000; Thornber *et al.*, 2003a; Desmarais & Segall, 2007). Eruptive activity continued, reaching steady-state effusive activity by mid-August 1997 (Garcia *et al.*, 2000; Thornber *et al.*, 2003a).

Episode 54 eruptive products are geochemically distinct from steady-state Pu'u'ō'ō'lavas (Thornber, 2001; Thornber *et al.*, 2003a, 2003b). Bulk rock compositions of Episode 53 lavas (22 September 1994 to 30 January 1997) average ~8.47 wt % MgO_{WR} (Fig. 2; Thornber, 2001; Thornber *et al.*, 2003b). Lavas of Episode 54 are unusual in that their compositions became *much* less magnesian over the course of the eruptive sequence, with terminal lavas reaching >51.25 wt % SiO_{2WR} and <5.75 wt % MgO_{WR} (Fig. 2;

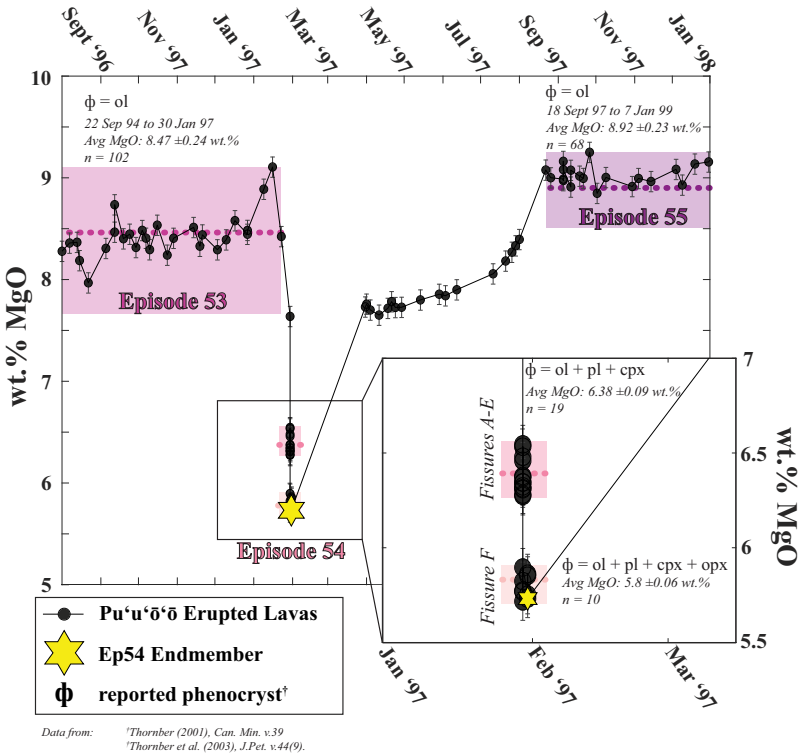

Fig. 2. Chemical evolution of lavas erupted immediately preceding, during, and after the Episode 54 event. Compositional and mineralogical data from Thornber (2001) and Thornber *et al.* (2003a). Shaded areas note the maximum and minimum extent of chemical variations within different groups of lavas, with the dashed line representing the average composition for that group.

Thornber, 2001; Thornber *et al.*, 2003a, 2003b). Lavas erupted during early Episode 55 became progressively more and more mafic, peaking at 9.25 wt % MgO_{WR}, before settling into steady-state eruptive activity for a decade (Fig. 2; Thornber, 2001; Thornber *et al.*, 2003a, 2003b).

Petrologic and geochemical evidence suggest that the low-wt % MgO_{WR} lavas erupted during Episode 54 were a result of mixing between basaltic magmas (e.g. 'olivine controlled') that had been recently supplied to shallow portions of Kīlauea's magmatic system and one (or more) previously intruded, partially solidified dike(s)—referred to here as 'rift-stored magmas' (Garcia *et al.*, 2000; Thornber *et al.*, 2003a; Thornber *et al.*, 2015; Walker *et al.*, 2019). Considering the likely geometry of the inferred dike complex underlying Kīlauea (Walker, 1986; Wallace & Anderson, 1998), the location of dikes emplaced in and around Nāpau Crater (Fig. 1; Thornber *et al.*, 2015), and the mixing of distinct magmas during other fissure eruptions along the ERZ (Gansecki *et al.*, 2019; Walker *et al.*, 2019), dikes intruding into each other appears to be a common occurrence beneath Nāpau Crater.

THE MAGMA CHAMBER SIMULATOR

Phase-equilibria models constructed in this study were accomplished using the Magma Chamber Simulator (MCS; Bohrson *et al.*, 2014, 2020). MCS is a thermodynamic model for computing phase equilibria, trace element, and isotope systematics in open systems undergoing concurrent or serial fractional crystallization (FC), assimilation of partial melts (A), digestion of stoped blocks (S), and/or magma mixing via magma replenishment/recharge (R). The MCS code, including documentation, examples, and instructional videos are available at http://mcs.geol.ucsb.edu (open access). The phase equilibria engine incorporated within the MCS software used in this study utilizes rhyolite-MELTS v1.1.0 (Gualda *et al.*, 2012; Ghiorso & Gualda, 2015). Symbols used in the text for MCS calculations are provided in Table 1. This study uses the MCS software to determine the source identity and thermodynamic state of the mixing endmembers involved in Episode 54 eruptions. We show that MCS can be used as a tool to complement real-time petrologic monitoring of ongoing eruptions by demonstrating its usefulness in modeling past eruptions.

Lavas erupted during Episode 54 were relatively crystal-poor (Thornber, 2001; Thornber *et al.*, 2003a), but were variably clotted with ~3 mm glomerocrysts of ol + pyx+pl (Thornber, 2001), indicating the presence of a multiply saturated phyric magma, in addition to the near-liquidus 'olivine-control' magmas that typically occupy the Kīlauea magma storage and transport system (Thornber *et al.*, 2003a; Orr, 2014; Gansecki *et al.*, 2019). Here, we create phase equilibria-guided mixing models simulating typical 'olivine-control' Kīlauea magmas mixing with a more evolved, partially crystalline, ol + pyx+pl-bearing rift-stored magma, characterizing the onset of Episode 54 (Thornber *et al.*, 2003a). Using MCS, the primary goal of this study is to constrain the composition and pre-eruptive thermodynamic state of the stored magma responsible for the presence of evolved melts and disequilibrium glomeroxenocrystic minerals within Episode 54 lavas. This is accomplished by comparing mineral assemblages and compositions *computed* using phase equilibria models to *observed* mineral compositions and assemblages from Episode 54 eruptive products (Thornber, 2001; Thornber *et al.*, 2003a). As our petrogenetic models provide likely compositions and proportions for mixing endmembers as inferred from previous geodetic (Owen *et al.*, 2000; Segall *et al.*, 2001; Desmarais & Segall, 2007) and geochemical

Table 1: Input Parameters for the Magma Chamber Simulator (Bohrson *et al.*, 2014; Bohrson *et al.*, 2020)

Input Parameters for Composite System	
Pressure:	**P (bars)**
fO_2 constraint	fO_2 buffer or initial Fe^{2+}/Fe^{3+}
Temperature decrement to subsystem M during approach towards T_{end}:	ΔT (°C)
Desired final temperature for end of MCS simulation:	T_{end} (°C)
M subsystem melt temperature for *j*th recharge event:	T_1^M, T_2^M, etc.
Ratio of mass of mafic recharge event to initial mass of rift-stored magma body:	M_j^{MME} / M_0^{Rmagma}

Magma body & Recharge magma subsystem inputs for MCS Simulations				
Subsystem	Initial bulk major oxide, trace element, and isotopic composition (for *i* components)	Temperature	Distribution Coefficient	Mass
Magma body (M)	X_0^M	initial T of subsystem T_0^M	D for each component & mineral phase	initial mass of subsystem (100% melt), M_0^M
Recharge, *j* events (R_j)	$X_{0,j}^R$	T_j^R	D for each component & mineral phase	mass of *j*th recharge increment, M_j^R

(Moore & Koyanagi, 1969; Jackson *et al.*, 1975; Thornber *et al.*, 2003a) studies, an equally important goal of this research is to establish if a self-consistent petrogenetic model of Episode 54 is also consistent with geodetically constrained volume displacements initially determined by Owen *et al.* (2000), and further refined by Segall *et al.* (2001) and Desmarais & Segall (2007).

VOLUME ESTIMATES OF EPISODE 54 ENDMEMBER MAGMAS

The events surrounding Episode 54 were captured in detail by a continuous Global Positioning System (GPS) network previously installed on Kīlauea volcano (Owen *et al.*, 2000; Segall *et al.*, 2001; Desmarais & Segall, 2007). Seismic tremor sequences occurred for ~8 hours preceding eruption onset, accompanied by drainback of Pu'u'ō'ō"s lava lake, deflation of the Kīlauea summit caldera, and seismic activity underneath Makaopuhi Crater—indicating the movement of magma at these three areas (Owen *et al.*, 2000; Thornber *et al.*, 2003a). During this time, extension within the southeastern flank of Kīlauea's edifice enabled a passive intrusion to form in a weakened area of the ERZ beneath Nāpau Crater (Owen *et al.*, 2000; Thornber *et al.*, 2003a). By the conclusion of this eruptive episode, the geodetic constraints suggest approximately 23 Mm^3 of magma had accumulated beneath Nāpau Crater, forming a roughly planar body that extended 5.15 km in length, 1.96 m in width, and ~2.24 km in the vertical extent (dipping so that the base of the intrusion was at ~2.4 km depth; see also Plate 2 in Owen *et al.*, 2000).

Point-source 'Mogi-style' models developed by Owen *et al.* (2000) and Segall *et al.* (2001) suggest the Episode 54 intrusion was sourced from three known reservoirs: (1) 1.50 Mm^3 of magma from the Kīlauea summit reservoir; (2) 1.20 Mm^3 of magma from a reservoir underlying Makaopuhi Crater; and (3) 12.7 Mm^3 of magma representing drainback from the Pu'u'ō'ō'lava lake. Dike volume estimates require the presence of an additional magma of unknown volume (Owen *et al.*, 2000) that geochemical studies suggest may be a cooler, multiply-saturated (ol + cpx + plag) magma, previously intruded into and stored within the rift zone (Garcia *et al.*, 2000; Thornber *et al.*, 2003a). This geodetic model was further refined by Desmarais & Segall (2007), who later provided revised estimates of intrusion along strike and down-dip lengths to 5.3 km and 2.7 km, respectively, with an additional 0.08 m of post-intrusion opening towards the base of the dike and transient deformation continuing for several months following the Episode 54 eruption. These estimates coincide with the findings of Segall *et al.* (2001), who demonstrate that two-thirds of the final dike volume had been intruded at the time of eruption, and that further volume accumulation continued after Episode 54, albeit at a much lower rate. From these geodetic estimates, we calculate that the volume of the intrusion at the time of the Episode 54 eruption was 22.91 Mm^3, and that the total final volume of the intrusion was 29.49 Mm^3, in good agreement with transient deformation models (Segall *et al.*, 2001; Desmarais & Segall, 2007). We calculate the maximum volume of rift-stored magmas beneath Nāpau Crater—Owen *et al.*'s unknown fourth component—to be ~7.51 Mm^3 by volume closure. The parameters obtained from the literature and the results of our volume calculations are presented in Table 2. For purposes of internal consistency, we have reported the above volumes with the same precision as Owen *et al.* (2000) and Desmarais & Segall (2007). A discussion of the assumptions and limitations of geodetic inversion models and the magnitude of their associated uncertainties is presented in Supplemental Item A. For the

Table 2: Dike and volume estimates for the Episode 54 intrusive event

[1]**Along-strike Dike Length (m):**	**5150**
[1]Vertical Dike Width (m):	2240
[1]Horizontal Dike Opening (m):	1.96
[1]Eruptive Volume Episode 54 (Mm^3):	0.30
[1]**Calculated Intrusion Volume at Time of Eruption (Mm^3):**	**22.91**
[1,3]Contribution from Pu'U 'O'o (Mm^3):	12.70
[1,3]Contribution from Makaopuhi (Mm^3):	1.20
[1,2]Contribution from Kilauea Summit (Mm^3):	1.50
Calculated Volume of low-MgO Magma Body (Mm^3):	**7.51**
[3]Calculated Post-Eruptive Transient Volume Accumulation (Mm^3):	6.58
Final Calculated Intrusion Volume (Mm^3):	**29.49**

[1] *Owen et al. (2000)*
[2] *Desmarais & Segall (2007)*
[3] *Segall et al. (2001)*

Table 3: Estimated Magma Volumes, Supply Rates, and Effusion Rates for early Episode 55

date range		*magma volume (Mm^3)*	*no. of days*	*est. magma supply rate (Mm^3/day)*	*no. of erupting days (w/ pauses)*	*est. effusion rate (Mm^3/day)*
31 Jan-24 Feb:	initial rapid refill of system following Ep54 eruption:	7.30	24.33	0.30		
25 Feb-2 Mar:	additional volume to magmatic system / intrusion:	4.00	8.00	0.50		
3 Mar-28 Mar:	additional volume to magmatic system / intrusion:	18.00	24.00	0.75	1.00	0.14
29 Mar-15 Apr:	additional volume to magmatic system / intrusion:	14.40	18.00	0.80	18.00	0.19
16 Apr-31 Jul:	additional volume to ERZ / magmatic system:	96.30	107.00	0.90	103.61	0.68
1 Aug-31 Dec:	additional volume to ERZ / magmatic system:	98.00	98.00	1.00	98.00	0.90

date range		*magma volume (Mm^3)*	*cumulative "refill" vol. (Mm^3)*	*cumulative intrusion vol. (Mm^3)*	*est. cumulative erupted vol. (Mm^3)*
31 Jan-24 Feb:	initial rapid refill of system following Ep54 eruption:	7.30	7.30	22.91	
25 Feb-2 Mar:	additional volume to magmatic system:	1.04	8.34		
	additional volume to Ep54 intrusive body:	2.96		25.87	
3 Mar-28 Mar:	additional volume to magmatic system:	14.57	22.91		0.14
	additional volume to Ep54 intrusive body:	3.29		29.16	
29 Mar-15 Apr:	additional volume to magmatic system:	10.67	33.57		3.41
	additional volume to Ep54 intrusive body:	0.33		29.49	
16 Apr-31 Dec:	additional volume to ERZ / magmatic system:	194.30	69.41		162.00

petrogenetic modeling, however, as the volume uncertainties are similar, the relative proportions of the different magmas involved are more important than their absolute values.

CONSTRUCTION OF THE MIXED MAFIC ENDMEMBER (MME) MAGMA

The geodetic (Owen *et al.*, 2000; Segall *et al.*, 2001; Desmarais & Segall, 2007) and petrologic (Garcia *et al.*, 2000; Thornber, 2001; Thornber *et al.*, 2003a) data support a magma mixing model for the Episode 54 lavas wherein an arrested and partially crystallized intrusive body (rift stored magma) interacted with distinct batches of mafic magma from the Kīlauea summit reservoir, a reservoir below Makaopuhi Crater, and drain-back from the lava lake at Pu'u'ō'ō'. For our petrogenetic modeling, we used published geochemical data—as detailed below—to estimate the major oxide composition of these three mafic magma sources and then combined them to create a single 'Mixed Mafic Endmember' (MME) composition (Table 4; green star in Fig. 4) in proportions constrained by the aforementioned geodetic relations. This MME is our best estimate of the mafic endmember involved in the mixing events interpreted to have occurred during Episode 54.

As magmas from Kīlauea's summit reservoir are reasonably homogenized prior to their arrival and subsequent eruption at the East Rift Zone (Edmonds *et al.*, 2015), we used the average steady-state composition of Episode 53 lavas erupted from Pu'u'ō'ō'(Thornber *et al.*, 2003a) to represent the Kīlauea summit component of the MME. Magmas derived from underneath Makaopuhi Crater were represented by a pumice—similar in composition to the Kīlauea summit component—from the 1968 Makaopuhi Crater eruption (Wright *et al.*, 1968). Finally, the largest ingredient (~83%) in the MME comes from magmas present in the Pu'u'ō'ō'conduit and underlying reservoir (Harris *et al.*, 1997; Owen *et al.*, 2000; Thornber *et al.*, 2003a) immediately preceding the onset of Episode 54, modeled using the last-erupted bulk lava sample from Episode 53 (KE53–1844; Thornber *et al.*, 2003b). Using these compositions and proportions constrained by geodetic measurements (see Table 2), the MME composition was generated by bulk mixing and renormalized to 100 wt % (Table 4). Fractional crystallization (FC) of the MME composition was modeled at $P = 0.05$ GPa using MCS, with initial $FeO/FeO_{tot} = 0.86$ and 0.5 wt % H_2O_i, without restricting fO_2 along a buffer (Supp. Item B). Despite some uncertainty in the exact compositions and volumes of the different MME components, the MME composition is dominated by the large volume drain-back from Pu'u'ō'ō'—suggested by geodetic measurements to provide the largest volume of melt (Owen *et al.*, 2000)—*and* the compositions of the three components of the MME are relatively similar (Wright *et al.*, 1968; Thornber *et al.*, 2003a, 2003b). Although our MME is not drastically different from the mafic endmember proposed by Thornber *et al.* (2003a), by adopting these compositional and geodetic constraints, we directly link our petrologic models to magmatic volumes.

Table 4: Major oxide compositions used in Episode 54 mixing models

	Kilauea Summit Component[1]	Makaopuhi Crater Component[2]	Pu'U 'O'o Drainback (Bulk Rock)[3]	Mixed Mafic Endmember (P = Bulk)[4]	Rift-Stored Magma (K63–2)[5]	Rift-Stored Magma (N68–4)[6]
SiO_2:	50.61	50.06	51.01	50.9	50.56	50.33
TiO_2:	2.4	2.62	2.44	2.45	2.65	2.66
Al_2O_3:	13.19	13.19	13.43	13.39	13.67	13.67
Fe_2O_3:		1.47			1.73	1.44
FeO:		9.81			9.52	9.88
FeO_{tot}:†	11.5	11.28	11.4	11.4	11.25	11.32
MgO:	8.47	8.49	7.64	7.79	7.64	7.71
MnO:	0.17	0.17	0.17	0.17	0.17	0.17
CaO:	10.83	10.73	11.06	11.01	10.99	10.89
Na_2O:	2.15	2.28	2.16	2.17	2.32	2.3
K_2O:	0.42	0.53	0.43	0.44	0.56	0.51
P_2O_5:	0.26	0.27	0.25	0.25	0.25	0.27
H_2O:‡	0.3	0.2	0.3	0.29	0.5	0.5
CO_2:‡	0.02	0.01	0.02	0.02	0.03	0.02

	Rift-Stored Magma (N68–8)[7]	Rift-Stored Magma (KE1–1)[8]	Rift-Stored Magma (KE1–49)[8]	Ep 54 Avg Fissures A-E[9]	Ep 54 Avg Fissure F[9]	Ep 55 Mafic Recharge Magma [10]
SiO_2:	50.39	50.3	50.98	50.92	51.2	50.39
TiO_2:	2.91	2.8	2.71	3	3.46	2.31
Al_2O_3:	14.35	13.76	14.04	13.88	13.72	13.05
Fe_2O_3:	1.35					
FeO:	10.08					
FeO_{tot}:†	11.43	11.2	11.27	11.7	12.1	11.51
MgO:	6.52	7.13	6.79	6.38	5.8	9.25
MnO:	0.17	0.17	0.17	0.17	0.17	0.17
CaO:	10.74	11.54	10.89	10.46	9.73	10.57
Na_2O:	2.47	2.23	2.35	2.52	2.72	2.1
K_2O:	0.59	0.53	0.52	0.6	0.71	0.39
P_2O_5:	0.28	0.32	0.29	0.36	0.43	0.25
H_2O:‡	0.5	0.5	0.5	—	—	0.7
CO_2:‡	0.01	0.02	0.02	—	—	0.02

[1]Episode 53 steady-state average composition, Table 1 in Thornber *et al.* (2003a). wt % H_2O and wt % CO_2 imputed from values given inMangan *et al.* (2014).
[2]Makaopuhi Crater Pumice M26, erupted 15 March 1965, Table 6 in Wright *et al.* (1968).
[3]Episode 53 KE53–1844, erupted 30 January 1997, in Thornber *et al.* (2003b). wt % H_2O and wt % CO_2 imputed from values given in Mangan *et al.* (2014).
[4]Calculated MME from mixing Components 1–3.
[5]Napau Crater basalt 2, erupted October 1963, in Moore & Koyanagi (1969).
[6]Fissure spatter erupted 13 October 1968, 0.5 km west of Napau Crater; see Table 2 in Jackson *et al.* (1975).
[7]Fissure spatter erupted 14 October 1968 from easternmost eruptive vent; see Table 2 in Jackson *et al.* (1975).
[8]Episode 1 lavas erupted 3 January 1983, in Thornber *et al.* (2003b). wt % H_2O and wt % CO_2 imputed from values given in Wallace & Anderson Jr. (1998) and Mangan *et al.* (2014).
[9]Average of Episode 54 Fissure A-E & Fissure F bulk rock compositions, from Thornber *et al.* (2003a).
[10]Episode 55 KE55–1924, erupted September 26, 1997, in Thornber *et al.* (2003b). wt % H_2O and wt % CO_2 imputed from values given in Wallace & Anderson Jr. (1998) and Mangan *et al.* (2014).
†For compositions where FeO and Fe_2O_3 were not measured using wet chemistry techniques, FeO_{tot} is reported.

IDENTIFICATION OF THE MORE EVOLVED, RIFT-STORED ENDMEMBER

Prior to the Episode 54 eruption, Kīlauea steadily effused near-liquidus, olivine-bearing, high (~8.47 wt %) MgO basaltic lavas for almost a decade (Thornber *et al.*, 2003a, 2003b). Episode 54 lavas are markedly different from those lavas erupted either before or after 30 to 31 January 1997: the more evolved lavas (avg. MgO = 6.38 wt %; Fig. 2) erupted from Fissures A-E contain complexly zoned phenocrysts and microphenocrysts of olivine (ol), clinopyroxene (cpx), and plagioclase (pl), occurring either as individual crystals or as glomerocrysts containing <80% interstitial glass; Fissure F lavas are petrographically similar to Fissure A–E lavas, but are even less magnesian (avg. MgO = 5.8 wt %; Fig. 2) and bear orthopyroxene (opx)—either as scarce, reversely zoned crystals or as exsolution lamellae within augite (Thornber, 2001; Thornber *et al.*, 2003a).

Although disagreement about the identity of the more evolved magmas required to produce Episode 54 bulk rock and mineral compositions (Garcia *et al.*, 2000; Thornber *et al.*, 2003a; Walker *et al.*, 2019) is still prevalent, there is consensus that mixing of more typical, mafic Kīlauea magmas (olivine-control; our MME) with a less magnesian, multiply-saturated magma *must* have occurred. The complex mixing history preserved in Episode 54 eruptive products was extensively documented by Thornber *et al.* (2003a), who suggested that a 'phenocryst-laden' (Thornber *et al.*, 2003a) and evolved magma body was rapidly reheated by and mixed with lower viscosity, higher-*T* mafic magmas, then erupted over a limited range of temperatures. Thornber *et al.* (2003a) found that this evolved, rift-stored mixing component was derived from nearly 40% fractionation of a bulk composition *equivalent* to an opx-bearing lava erupted from the Lower East Rift Zone in 1955. Given that no opx-bearing lavas have erupted in Nāpau Crater,

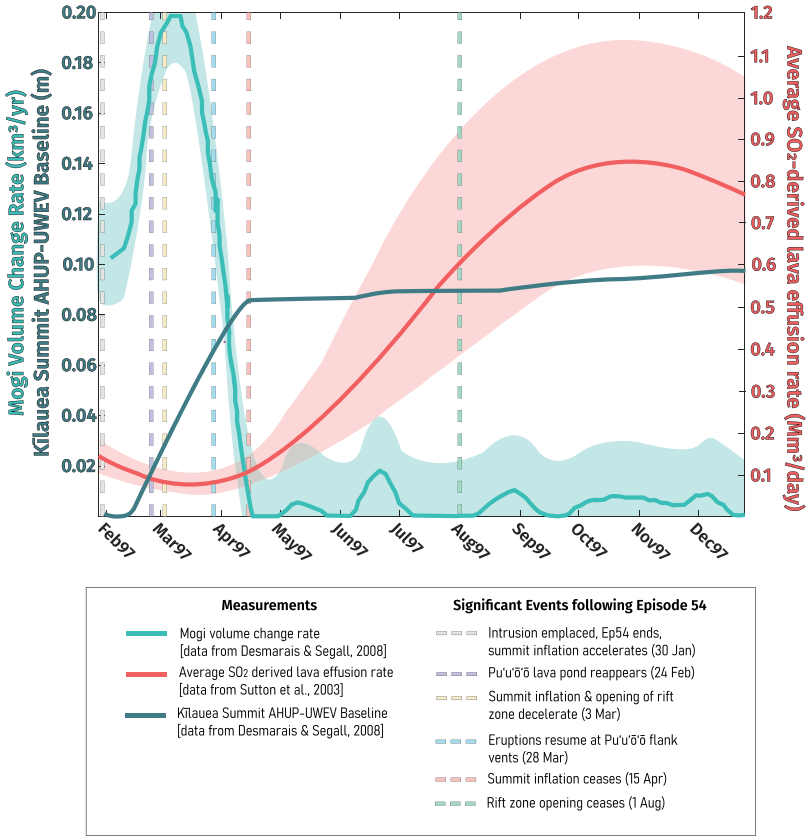

Fig. 3. Variations in rates of magma volume accumulation and geodetic baseline measurements at Kīlauea's summit caldera (*from* Desmarais & Segall, 2007), and fast Fourier transform (FFT)-smoothed lava effusion rates based on SO_2 emissions (*from* Sutton *et al.*, 2003) for the recovery period following Episode 54 and early Episode 55. Significant events observed as Kīlauea's edifice adjusted to the newly emplaced Episode 54 intrusion (*from* Desmarais & Segall, 2007) are noted by dashed vertical lines.

they suggested that an equivalent composition might be derived from magmas intruded into the Nāpau Crater region during 1963, 1968, or 1983 (Garcia *et al.*, 2000; Thornber *et al.*, 2003a; Walker *et al.*, 2019). Conversely, Garcia *et al.* (2000) and Walker *et al.* (2019) maintain that two different bulk compositions that existed at the time as discrete, molten magma bodies located beneath Nāpau Crater are responsible for the anomalous compositions of Episode 54 lavas. Specifically, Walker *et al.* (2019) argues that leftover melts from the initial 1983 intrusion are the low-MgO mixing component that produced Fissure A-E lavas, and that Fissure F lavas show no evidence of magma mixing and are *themselves* the erupted portion of a discrete rift-stored, low-MgO magma body. This study tests these hypotheses by constructing a series of phase-equilibria models to compare model results to measured Episode 54 lava and mineral compositions, with the goal of discerning between the different proposed low-MgO endmember compositions.

After reviewing available literature and examining fissure locations in and around Nāpau Crater (Fig. 1; Thornber *et al.*, 2003a; Thornber *et al.*, 2015; Walker *et al.*, 2019), we examined five potential basalts for their suitability as the arrested dike (and starting composition for our FC models): K63–2, erupted from fissures within Nāpau Crater during October 1963 (Moore & Koyanagi, 1969); N68-4 and N68-8, erupted in October 1968 (Jackson *et al.*, 1975); and KE1-1 and KE1-49, erupted at the onset of the Pu'u'ō'ō'eruption in 1983 (Thornber *et al.*, 2003a, 2003b). The 1955 opx-bearing composition (TLW 67-34 from Wright & Fiske, 1971) was not tested as a potential endmember because it–or any potential liquids derived from a similar composition–are too deficient in wt % Al_2O_3 to serve as a mixing endmember to produce Ep54 lavas.

To constrain potential compositions of the evolved dike at the time of mixing, and therefore, determine whether they might represent the evolved mixing endmember during the Episode 54 eruption, we first used MCS to model the evolution of dike liquids as they fractionally crystallize (ornamented dashed lines in Fig. 4, see also Supp. Figure B1). Of the examined compositions, MCS fractionation models for the lavas erupted from Napau Crater in October 1968 (N68-4) best reproduce the compositions and proportions of ol, pyx, and pl found in glomerocrysts from Episode 54 lavas (Supp. Figure B2) (Thornber, 2001; Thornber *et al.*, 2003b). N68-4 is a sample of melt spatter collected in October 1968 with a roughly peritectic composition (see Rhodes, 1995), which is petrogenetically related to N68-8, a second sample from the same eruptive sequence. Jackson *et al.* (1975) determined that the composition of N68-8 can be reproduced by fractionation of the 1961 Kilauea summit magma compositions, *and* that N68-8 is an endmember magma that syneruptively mixed with resident summit magmas to produce magmas similar in composition to N68-4. Thus, N68-4 is more representative of the post-eruptive dike composition than N68-8, reinforcing it as a better choice for the 1968 magma composition selected as our best reference LLD. We also note that this composition is more similar to lavas erupted from Kīlauea during periods of steady-state activity than most of the other compositions examined. Consequently, dike N68-4 was selected as the best reference LLD (liquid line of descent) for construction of the more evolved, rift-stored endmember.

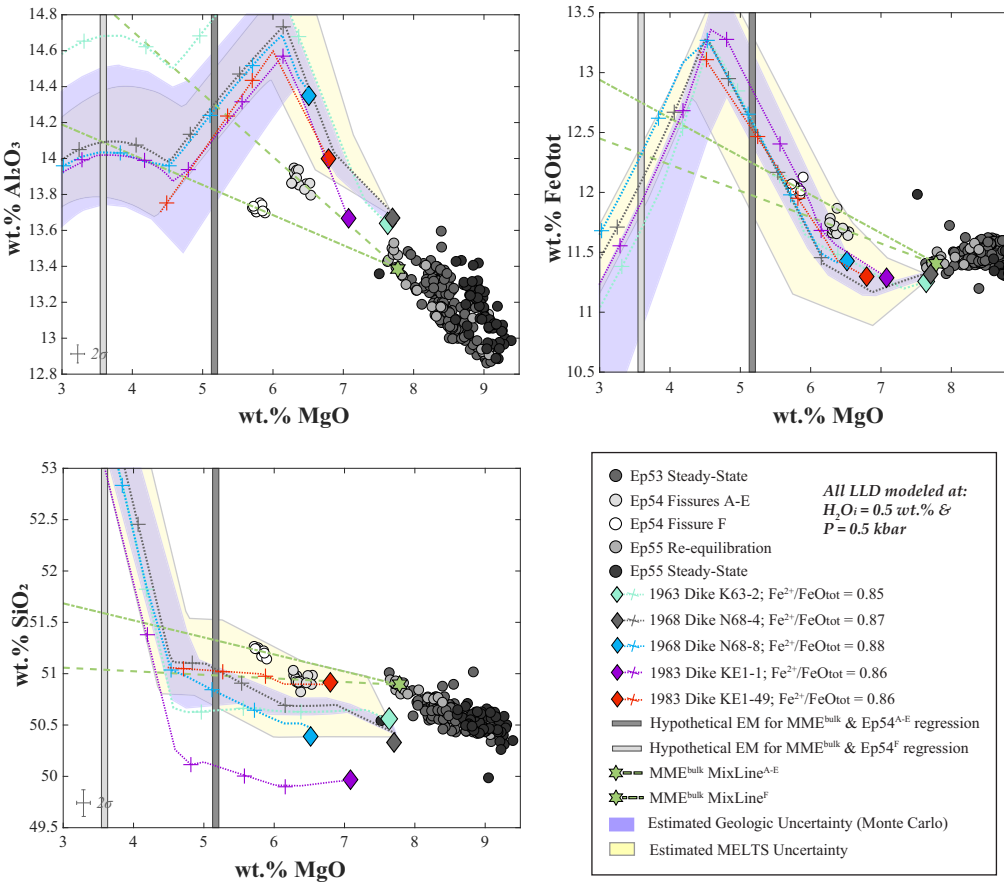

Fig. 4. Variations in melt compositions produced by fractional crystallization (FC) models of five candidate low-MgO endmember (arrested dike) compositions. For compositions where ferric-ferrous ratios were determined using wet chemistry techniques (see Table 4), log fO_2 was calculated using Eqn. 7 of Putirka (2016). Of the five dikes tested, mineral compositions and modal abundances from Episode 54 lavas are best reproduced by FC of Dike N68–4, using the Magma Chamber Simulator (Bohrson *et al.*, 2014, 2020). Mixing lines (l^{mix}) were constructed by linear regression of the mixed mafic endmember (MME) with measured lava compositions from Fissures A-E and Fissure F, respectively. The wt % MgO for each low-MgO endmember is determined by the intersection between l^{mix} and the LLD on the Al_2O_3 vs. MgO plot; wt % MgO for the resultant hypothetical endmember compositions are denoted by grey vertical bands. Uncertainty fields for MELTS models and variations in geologic parameters were calculated for the fractionation model of N68–4, our preferred parental dike composition.

Intensive model parameters for our FC models were selected by evaluating a suite of exploratory models (Supp. Item. C) that varied *P*, FeO/FeO_{tot}, and wt % H_2O. These models were constructed to better understand how changing such parameters may affect the phase equilibria model results of arrested dike compositions. We estimate the amount of uncertainty within our MCS models for these intensive parameters (the 'geologic' uncertainty that can be expected in natural systems) by randomly sampling (n = 50) a randomly generated normal distribution of reasonable values for each of these parameters, and recording maximum variations in the resultant LLD (purple uncertainty bounds in Fig. 4; see also Supp. Item C). We attempt to quantify uncertainties of the rhyolite-MELTS phase-equilibria calibration used in our MCS models by understanding the difference in experimental versus modeled compositions (Supp. Item C), although quantifying exact uncertainties of phase-equilibria models are beyond the scope of this study (yellow uncertainty bounds in Fig. 4; Paul Asimow, *pers. comm.*).

When comparing wt % MgO versus wt % Al_2O_3 for the data set, the geochemical variations depicted in Fig. 4 (see also Supp. Figure B1 for the full suite of bivariate diagrams) illustrate the orthogonal relationships between any modeled LLD and each of the calculated l^{mix} regression lines. Lavas erupted from Fissures A–E and Fissure F are compositionally distinct (Figs. 2 and 4), suggesting that the mixed mafic endmember (MME; green star in Fig. 4) mixed with two different compositions—one more evolved (Fissure F) than the other (Fissures A–E). The dashed green lines (l^{mix}) in Fig. 4 are calculated mixing lines between our MME composition and the whole rock average compositions from the Fissure A–E and Fissure F eruptions (as given by Thornber *et al.*, 2003a). Hence, for any LLD, there should exist two different melt compositions that can serve as the low-MgO mixing endmembers for distinct lavas erupted from Fissures A–E and Fissure F (Langmuir *et al.*, 1978).

To estimate the extent to which N68-4 had fractionated between the time it was emplaced in 1968 until the Episode 54 eruption ~28 years later, we constructed two different mixing lines (l^{mix}). l^{mix} are regression lines between the MME composition (green star in Fig. 4) and the average lava compositions from Fissures A-E (AE^{avg} in Table 4; Thornber *et al.*, 2003a) and Fissure F (F^{avg} in Table 4; Thornber *et al.*, 2003a). Each l^{mix} was projected to its intersection with the modeled LLD for N68-4, represented by blue asterisks in Fig. 6. The intersection between each l^{mix} and the LLD in MgO–Al_2O_3 space was used to determine how fractionated the rift-stored dike was at the time of mixing, for both $A\text{-}E^{avg}$ *and* F^{avg}. In MgO–Al_2O_3 space, the l^{mix} for $A\text{-}E^{avg}$ intersects N68-4's LLD at ~5.1 wt % MgO, and the l^{mix} for F^{avg} intersects at ~3.5 wt % MgO, as represented by the vertical gray

lines in Fig. 4. Ideally, each l^{mix} would intersect the LLD for every major element at the same wt % MgO, but in reality, this is not the case; the intersection between the l^{mix} and the LLD fall at slightly different wt % MgO for each element. At no point along the LLD for any of our potential dike compositions (Fig. 4; see also Supp. Figure B2) does there appear to be a single composition that could be used as an evolved endmember to match all elements for either A-E^{avg} or F^{avg}. This is likely due to the analytical uncertainties in the original analyses of the dike compositions, the geologic uncertainties in the model (e.g. FeO/FeO_{tot}, wt % initial H_2O, P; purple color fields in Fig. 4), and inherent uncertainties within the phase-equilibria models (pale yellow color fields in Fig. 4), which we have estimated in Supp. Item C and illustrated in Figs. 4-5. The compositional similarities between Kilauea basalts over its ~300 000 year lifetime are well-documented (Garcia, 2003; Helz *et al.*, 2014; Clague & Sherrod, 2014), and it is likely melt compositions exist that *do* satisfy the linearity requirements necessitated by mixing processes (Langmuir *et al.*, 1978). Thus, our solution to this problem cannot be a *unique solution*. But, we can find *a solution* by adjusting our endmember composition within the limits of the uncertainties as described below.

Given the model uncertainty (purple and pale-yellow color fields in Fig. 4; see also Supp. Item C) we adjusted the mixing endmember compositions predicted by the intersection between the l^{mix} and LLDs to values that satisfy *both* the linearity requirements of bulk mixing (Langmuir *et al.*, 1978) and lie within calculated uncertainty of the modeled LLD. These adjusted compositions were then used as the low-MgO endmembers for our Episode 54 mixing models. In selecting mixing endmembers and proportions, we exercised the constraint that the entire rock composition (i.e. *all* oxides) must reflect identical proportions of the identified endmembers (Langmuir *et al.*, 1978; von Engelhardt, 1989). We, therefore, defined two best-fit fractionated rift stored magma endmember compositions—one falling on the l^{mix} for A-E^{avg}, and the other falling on the l^{mix} for F^{avg}—by using the LLD as a reference point for least squares regression.

For any given MgO, the intersection between the l^{mix} and the LLD predicts a concentration for each major oxide. For the Fissure A–E and Fissure F rift stored magma endmembers, we adjusted wt % MgO to find a single value, where the predicted concentrations for each major element along the l^{mix} line at the chosen wt % MgO plots as close as possible to the intersection between l^{mix} and the LLD produced by fractionation of N68–4 (i.e. we minimized the sum of the residuals between the predicted major oxide concentration along l^{mix} and the intersection of l^{mix} and the LLD). This was done twice—first by minimizing the squared residual of wt % MgO, and second by minimizing the sum of squared residuals for all oxides. The singular data point along l^{mix} that satisfies both these requirements is considered to be the most likely low-MgO endmember responsible for forming the hybrid compositions. For each l^{mix}, concentrations of major oxides other than wt % MgO were then fixed as that oxide's l^{mix} value corresponding to the selected wt % MgO (Fig. 4; Supp. Fig. C1).

The above method results in two individual low-MgO melts: a 5.28 wt % MgO melt needed to reproduce A-E^{avg}, and a 4.43 wt % MgO melt needed to reproduce F^{avg}. Complete bulk magma compositions for both low-MgO endmembers are given in Table 5, and illustrated in Fig. 5.The 'best fit' MgO content of 4.43 wt % for the Fissure F low-MgO endmember is significantly higher than the ~3.5 wt % MgO value noted above, based only on the intersection between l^{mix} and the LLD intersect in MgO–Al_2O_3 space. However, the higher MgO is consistent with the paucity of Fe–Ti oxides in Episode 54 lavas (Thornber *et al.*, 2003a), as the N68-4 models reach ilmenite saturation around 4.5 wt % MgO. Although it is possible that any ilmenite crystals were completely reabsorbed, the short duration of Episode 54 (<24 hrs; Harris *et al.*, 1997; Owen *et al.*, 2000) and preserved disequilibrium mineral assemblage of the erupted lavas imply otherwise. We instead consider it likely that the evolved endmembers must have had $\gtrsim$4.5 wt % MgO, consistent with our best fit model.

Using the described least squares method, we find that the stored magma body responsible for the evolved nature of Episode 54 lavas (Table 5) was likely derived from ~23% (Fissures A–E) to ~35% (Fissure F) fractionation of an intruded magma *very* similar in composition to sample N68–4 (Jackson *et al.*, 1975)—a triply saturated tholeiitic lava collected from the October 1968 fissure eruption (and associated intrusion) at Nāpau Crater. We emphasize that although the regressed endmember compositions do not fall exactly on the LLD for dike N68-4 (Fig. 6), the selected MgO—and, therefore, the degree to which the dike has fractionated—are constrained by the orthogonal relationship between the LLD and l^{mix}, and lie within estimated geologic and phase-equilibria uncertainties (Supp. Item C).

PHASE-EQUILIBRIA MAGMA MIXING MODEL: METHODS AND RESULTS

After determining the best-fit endmember compositions needed to reproduce A-E^{avg} and F^{avg}, we conducted two series of numerical experiments to constrain the relative proportions of liquid and crystals of the rift-stored magma at the time of the Episode 54 mixing event. This model envisions a two-step process, where an intrusion with a composition similar to N68-–4 intruded and fractionated along the LLD as described in the previous section, with all solid products being removed from the system (this stage involves the 23–35% fractional crystallization, as outlined in the preceding section). In a second stage described herein, the crystal-free, now-fractionated melt continues to cool and crystallize in-situ prior to the Episode 54 eruption. The crystal cargo of this now-fractionated magma was not removed prior to its mixing with the MME, and therefore, impacts the thermodynamics of the mixing event. We model this second stage as a closed-system process, wherein the rift-stored low-MgO magmas are modeled as bulk compositions of liquid + crystals that mix with the MME melt composition. For both the Fissure A–E and Fissure F low-MgO endmembers, equilibrium crystallization of each residual (fractionated) liquid composition was modeled over the range of T correlating with crystal contents from 20–80% (φ = 20–80), at P = 0.1 kbar. A resulting mushy, low-MgO endmember was then mixed with the near-liquidus ($\varphi < 1$) MME; mixing proportions required to reproduce A-E^{avg} and F^{avg} (Table 4; Thornber *et al.*, 2003a) were determined by linear combination, and are given in Table 5 along with other input parameters for each numerical experiment. Full MCS results, supplemental figures, and individual MCS output files are provided in Supp. Item D. An illustrative guide to our two-stage MCS model is presented in Fig. 5.

The resultant bulk hybridized magma compositions (Fig. 6) are required to overlap the average Episode 54 lava compositions by the method we used to determine the rift-stored endmember and mixing proportions. The MCS models are useful because mineral compositions in equilibrium with the hybrid lavas produced in the Recharge + Fractional Crystallization (RFC) models can be compared with observed mineral compositions from erupted Episode 54 lavas to estimate the crystallinity of the low-MgO magma

Table 5: Major oxide compositions of endmember magma compositions and selected input parameters for Episode 54 mixing models

	Mixed Mafic Endmember (MME)[1]	Dike X[2] to match MME & A-E lavas	Dike X[3] to match MME & F lavas
SiO_2:	50.76	50.64	51.03
TiO_2:	2.45	3.39	4.11
Al_2O_3:	13.35	14.14	13.84
FeO_{tot}:	11.37	11.86	12.37
MgO:	7.76	5.28	4.43
MnO:	0.17	0.17	0.17
CaO:	10.98	9.99	8.80
Na_2O:	2.16	2.75	3.08
K_2O:	0.43	0.72	0.90
P_2O_5:	0.25	0.40	0.51
H_2O:	0.29	0.65	0.76
CO_2:	0.02	0.02	0.02
% fractionated from initial X:	0.03	23.25 ± 3.25	34.93 ± 5.15
f_{mix} low-MgO:	—	0.57 ± 0.01	0.60 ± 0.00
P (kbar):	—	500	100
M^{MME} / $M^{rift\text{-}stored}$:	—	0.75	0.67
T^M (°C):	1181	—	—
ΔT (°C):	5	—	—
20% Xlln T^R (°C):	—	1096	1084
30% Xlln T^R (°C):	—	1087	1076
40% Xlln T^R (°C):	—	1075	1067
50% Xlln T^R (°C):	—	1057	1053
60% Xlln T^R (°C):	—	1031	1036
70% Xlln T^R (°C):	—	994	1012
80% Xlln T^R (°C):	—	948	970
T_{stop} (°C):	900	900	900

[1]Calculated MME from Table 2 renormalized to 100 wt % in rhyolite-MELTS v1.1.0, with initial $FeO/FeO_{tot} = 0.87$.
[2]Best-fit felsic endmember to reproduce Fiss A-E lavas, renormalized to 100 wt % in rhyolite-MELTS v1.1.0, with initial $FeO/FeO_{tot} = 0.87$.
[3]Best-fit felsic endmember to reproduce Fiss F lavas, renormalized to 100 wt % in rhyolite-MELTS v1.1.0, with initial $FeO/FeO_{tot} = 0.87$.

at the time of the mixing event. Thornber (2001) and Thornber *et al.* (2003a) report that Episode 54 lavas are highly vesiculated and relatively aphyric, containing <5 vol % phenocrysts of ol, pl, cpx, and rare cpx + pl glomerocrysts. Thornber *et al.* (2003a) also report that groundmass crystallinity of Episode 54 lavas varies considerably, with glass making up anywhere between ~1 and ~80 vol % of the matrix. Additionally, Fissure F lavas contain both rare opx phenocrysts and high-Mg# opx lamellae within cpx phenocrysts, requiring that the low-MgO endmember for Fissure F was two-pyx saturated.

We note that the petrographic descriptions of Garcia *et al.* (2000) greatly differ from those of Thornber *et al.* (2003a). In particular, Garcia *et al.* (2000) report only very rare ol and pl phenocrysts in their Episode 54 lavas, with rare microphenocrysts of ol + pl + cpx; no glomerocrysts, cpx phenocrysts, or opx are reported. This discrepancy in reported mineral assemblages may be due to inadequate sampling, as only a single sample from each Episode 54 fissure was reported by Garcia *et al.* (2000), whereas Thornber (2001) and Thornber *et al.* (2003a) examined a total of 29 samples from Episode 54. Furthermore, the ol + pl + cpx + opx mineral assemblage is depicted in backscattered electron images of Episode 54 lavas (Thornber *et al.*, 2003a). We, therefore, attempt to reproduce the more evolved mineral assemblage reported by Thornber *et al.* (2003a) in our phase-equilibria models. Mineral compositions computed in our mixing models are presented in Fig. 6 and discussed in detail below; full results of our mixing models are provided in Supp. Item D.

DISCUSSION

Previous studies have addressed the issue of magma mixing in the petrogenesis of Episode 54 eruptive products (Garcia *et al.*, 2000; Thornber *et al.*, 2003a; Walker *et al.*, 2019). In addition to reexamining the mixing processes responsible for Episode 54 lava compositions, the current study incorporates revised geodetic constraints, considers measured lava effusion rates, and adds a phase-equilibria perspective to the volcanologic picture. Indeed, the advantage of a phase-equilibria study lies in the ability to compare more than just bulk rock geochemistry—modal abundance of phases and their compositions can be evaluated as well to obtain a more complete view. Here, we review the petrologic constraints on the low-MgO endmember based on the mineralogy and phase compositions of Episode 54 lavas, and discuss how these results—combined with our MCS modeling—constrain the composition and pre-eruptive state of the rift-stored magma body.

Determining the minerology and crystallinity of the shallow, rift-stored magma body

Decreasing specific enthalpies dictate the mineral phases and compositions that will be thermodynamically stable as the low-MgO endmember becomes more crystalline (Table 6). Therefore, we can use mineral compositions produced in the MCS forward models to constrain the pre-eruptive state of the low-MgO rift-stored magmas. Although we utilize a thermodynamic model (MCS; Bohrson *et al.*, 2020) to model a dynamic process (the rapid

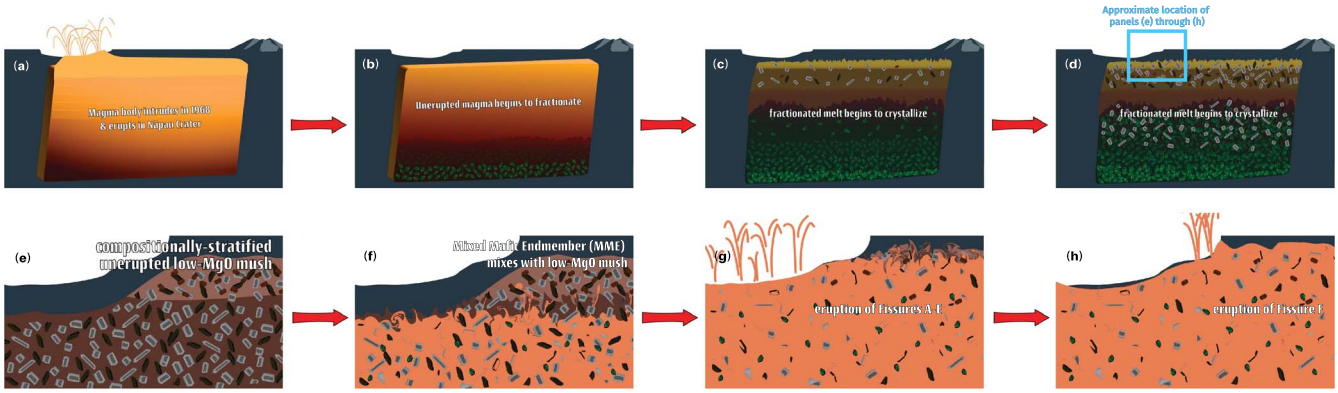

Fig. 5. A step-by-step illustrative guide to the processes modeled in our two-stage MCS models. In (a) a magma body intrudes into the region underlying Nāpau Crater and erupts. In (b), the unerupted magma undergoes fractional crystallization and the resultant residual liquids form a compositionally (and, therefore, density)stratified magma body, as posited by Thornber *et al.* (2003a). The uprift eruption of Mauna Ulu (1969–1971; Wright & Klein, 2014) limited the amount of heat delivered by fresh magma to the Nāpau Crater region, likely initiating solidification of the now-stratified intrusion as depicted in (c) and (d), and it crystallizes into a multiply-saturated mush (e) between 1968 and 1997. At the onset of Episode 54, mafic magma (our Mixed Mafic Endmember; MME) from different sources within the Kīlauea edifice mix with and entrain the low-MgO mush (f). Over the next 22 hours, Fissures A-E erupt (g), followed by Fissure F (h). Our MCS models are similarly two-stage: (a) through (c) illustrate the fractional crystallization process in the first stage of our models, while (d) thorough (h) illustrate the equilibrium crystallization and mixing that are simulated in the second stage of our phase-equilibria models.

mixing of different magma batches), we are effectively examining the equilibrated, pre-mixing state of the endmember magmas—rendering MCS an appropriate diagnostic tool.

State of the rift-stored low-MgO endmember as constrained by fissure A-E forward models

The results of the second-stage MCS forward models combined with major element trends demonstrate that mixing between our MME and a bulk composition produced by ~23% fractionation of a basalt similar to one intruded into the Nāpau crater region in 1968 (N68-4; Jackson *et al.*, 1975) generates a low-MgO endmember magma that reproduces the mineral assemblages and compositions present in lavas erupted from Fissures A-E. Our model predicts this result using a mixing proportion of 57% low-MgO component and 43% MME. Here we look in detail at how MCS mineral compositions for both the low-MgO magma and resultant hybrid lavas can be compared to the observed phenocryst compositions in the Episode 54 lavas to constrain the degree of crystallinity of the rift-stored magma immediately preceding the Episode 54 mixing event.

Fissure A-E lavas are triply saturated, containing ol, cpx, and pl (Fig. 7, see also Thornber *et al.*, 2003a). Ol is a stable hybrid phase in the MCS models when the low-MgO endmember is <70% crystalline, and is replaced by pigeonite (low-Ca pyroxene) when the crystallinity of the low-MgO endmember increases to 80%, whereas augite remains a stable phase in all MCS models. As depicted in Fig. 6, Thornber (2001) and Thornber *et al.* (2003a) report two populations of Fissure A-E ol: a) higher-$Fo_{(81–84)}$ phenocrysts and microphenocrysts in equilibrium with the different mafic magmas sourced for the Episode 54 intrusion (dark gray circles), and b) lower-$Fo_{(74–80)}$ microphenocrysts and syn-eruptive skeletal crystals and epitaxial overgrowths crystallized from the hybrid lavas (intermediate gray circles). Similarly, higher-$An_{(77–80)}$ pl in equilibrium with lavas more mafic than those erupted during Episode 54 (dark gray circles in Fig. 7) were found alongside those with lower $An_{(60–69)}$ which crystallized from hybrid melts (intermediate gray circles in Fig. 7; Thornber *et al.*, 2003a). At low-MgO endmember crystallinities up to 50%, our MCS model results (Table 6a) reproduce ol and augite compositions in equilibrium with hybrid melts; this relationship is shown on Fig. 6 in the compositional overlap between low to moderate-crystallinity MCS results (red to yellow squares) and the intermediate gray circles interpreted to represent crystals in equilibrium with the hybrid magma erupted at fissures A-E. For those phase-equilibria models where the low-MgO endmember is ≥40% crystalline, MCS-produced pl compositions overlap a subset of the measured plagioclase interpreted to be in equilibrium with the hybrid magma (intermediate gray circles). Fig. 6 shows that while compositional overlap is evident between the measured and modeled plagioclase, calculated *T* estimates of crystallization are higher for measured crystals (based on geothermometry found in Thornber *et al.*, 2003a) than are predicted in our forward models. This disparity likely reflects uncertainties in the MCS forward models (Supp. Item C) and the geothermometry estimates (Thornber *et al.*, 2003a; Wieser *et al.*, 2023); we note that even the 'best' pl-liquid geothermometer currently available (Waters & Lange, 2015) still has an uncertainty of ±12°C, which is about half the difference between our modeled hybrid magma *T* and the pl crystallization *T* estimated by Thornber *et al.* (2003a). For the rift-stored magma body, an upper limit of 50% crystallinity is supported by the absence of Fe–Ti oxides or opx in Fissure A-E lavas (Thornber *et al.*, 2003a); Fe–Ti oxides are produced as stable MCS hybrid phases for those models where the low-MgO endmember is ≥60% crystalline, and opx is stable in the low-MgO endmember if it is ≥50% crystalline. The lack of these phases in erupted Fissure A–E lavas could be due to sampling bias, and so the trace amounts of opx in the modeled low-MgO endmember at $\varphi = 50\%$ are geologically plausible. Disequilibrium textures and mineral compositions may not necessarily be reflected in the results of an equilibrium MCS model.

Finally, we can also use the compositions of phases that crystallize from the low-MgO endmember in the MCS models prior to mixing to further constrain the magma's thermodynamic state immediately preceding the mixing event. Potentially antecrystic cpx recovered from Fissure A–E lavas (lightest gray circles in Fig. 7; Thornber *et al.*, 2003a) can be reproduced by equilibrium crystallization of the low-MgO endmember (diamonds in Fig. 7) over a range of ~1094–1056°C (Fig. 7), correlating with $\varphi = 20–50\%$. Further, measured pl from Fissure A-E lavas (gray circles) form a linear trend from An_{61} to An_{81}, where the low An grains (lightest

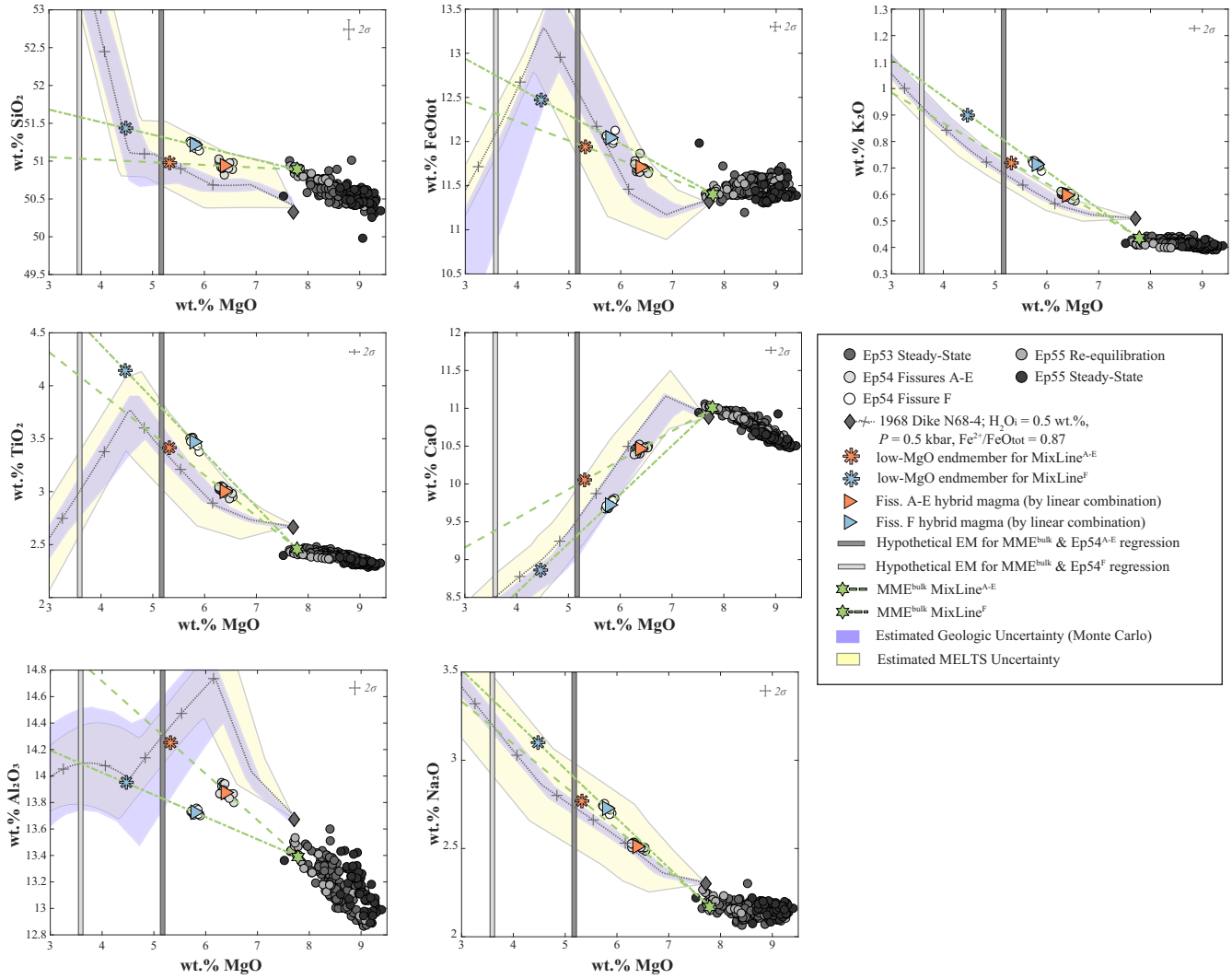

Fig. 6. Constructed low-MgO endmember compositions (SSR-minimized method) and results of Episode 54 mixing models as calculated by linear combination. Note that although the low-MgO endmember compositions do not lie exactly along the liquid line of descent, they are within either analytical, geologic, or model uncertainty, with the exception of K_2O (see text of Supp. Item C for further explanation). Mixing endmember compositions predicted by the intersection between each l^{mix} and the LLD (grey vertical bars) were adjusted to values that satisfy both the linearity requirements of bulk mixing (Langmuir *et al.*, 1978) and lie within the estimated uncertainty fields (as discussed in Supp. Item C) by minimizing *both* the squared residual of wt % MgO and the sum of squared residuals for all oxides; adjusted low-MgO endmember compositions are represented by asterisk symbols. The singular data point along l^{mix} that satisfies both these requirements is considered to be the most likely low-MgO endmember responsible for forming the hybrid compositions (right-facing triangles).

gray circles) may be antecrysts from the rift-stored magma, and the highest An grains (dark gray circles) are likely antecrysts from the mafic recharge magmas (Fig. 7; Thornber *et al.*, 2003a). Equilibrium crystallization of the low-MgO endmember at T = 1069°C (φ = 50) reproduces An_{61} pl, although estimates of crystallization *T* (lightest gray circles) are higher than our MCS model results (Fig. 7). These additional constraints reinforce our finding that prior to 29 January 1997, the rift-stored magma body was a magmatic mush consisting of 40–50% crystals.

State of the rift-stored low-MgO endmember as constrained by fissure F forward models

Results of the MCS forward models demonstrate that a bulk composition produced by ~35% fractionation of N68-4 (Jackson *et al.*, 1975) can generate a low-MgO endmember magma that reasonably reproduces the mineral assemblages and compositions present in Fissure F lavas when mixed with the MME. In this case, the hybrid magma is ~60% low-MgO endmember component and ~40% mafic endmember component. Mineral compositions produced in the second-stage MCS forward models further constrain the state of the evolved intrusion that mixed to form Fissure F lavas, and suggest that this low-MgO endmember was ~40% crystalline immediately preceding the Episode 54 mixing event.

Like the lavas that preceded them, Fissure F lavas are triply saturated, bearing equilibrium ol, cpx, and pl (Fig. 7). Ol is a stable hybrid phase in the MCS models when the low-MgO endmember is ≤50% crystalline at the time of mixing, pigeonite is present in hybrid lavas for those MCS models where the low-MgO endmember is 40% to 70% crystalline, and opx can only be produced in MCS as a hybrid phase when the low-MgO endmember is >70% crystalline (Fig. 7, Table 6b). Ol with $>Fo_{80}$ are sourced from mafic recharge magmas (dark gray circles; Thornber *et al.*, 2003b), and so we do not expect them to be equilibrium phases in model hybrid lavas. The least forsteritic ol measured in Fissure F lavas

Table 6a: Mineral assemblages and compositions produced by MCS forward models for Fissure A-E lavas and resultant enthalpies of formation for each equilibrated mineral assemblage

MCS Run	Rift-Stored Magma		Phases Present in Rift-Stored Magma	Fo (ol)	Mg (cpx1)	Mg (cpx2)	An (pl)	Mg (opx)	ΔfH^0_{dike} (kJ/mol)
	Xllnty	T (°C)							
20JulB	19.64	1094	cpx + pl + mt		76.85		66.00		−1214
20JulC	29.15	1088	2cpx + pl + mt + il + fl		75.45	69.23	65.00		−1218
20JulA	39.42	1080	2cpx + pl + mt + il + fl		73.87	67.46	63.00		−1223
20JulD	49.42	1069	opx + cpx + pl + mt + il + fl		71.30		60.61	68.82	−1228
20JulF	58.83	1056	opx + cpx + pl + mt + il + fl		69.23		57.58	66.31	−1232
20JulG	68.87	1036	opx + cpx + pl + mt + il + ap + fl		66.38		54.55	62.57	−1238
20JulH	78.99	1004	opx + cpx + pl + mt + il + ap + fl		62.61		51.02	58.51	−1245
MCS Run	**Hybrid Lavas**		**Phases Present in Hybrid Lavas**	**Fo (ol)**	**Mg (cpx1)**	**Mg (cpx2)**	**An (pl)**	**Mg (opx)**	ΔfH^0_{hyb} (kJ/mol)
	Xllnty	T (°C)							
20JulB	7.96	1123.13	ol + cpx + pl + fl	75.76	80.00		70.71		−2814
20JulC	12.31	1117.17	ol + cpx + pl + fl	74.00	79.09		69.70		−2819
20JulA	17.11	1110.17	ol + cpx + pl + fl	73.00	78.18		68.00		−2826
20JulD	22.15	1102.20	ol + 2cpx + pl + fl	71.00	76.58	71.26	67.00		−2832
20JulF	27.95	1095.79	ol + 2cpx + pl + mt + fl	69.70	76.15	70.24	66.00		−2838
20JulG	35.71	1090.85	ol + 2cpx + pl + mt + il + fl	68.69	75.45	69.23	65.66		−2846
20JulH	44.50	1083.52	2cpx + pl + mt + il + fl		74.55	67.86	64.00		−2856

Table 6b: Mineral assemblages and compositions produced by MCS forward models for Fissure F lavas and resultant enthalpies of formation for each equilibrated mineral assemblage

MCS Run	Rift-Stored Magma		Phases Present in Rift-Stored Magma	Fo (ol)	Mg (cpx1)	Mg (cpx2)	An (pl)	Mg (opx)	ΔfH^0_{dike} (kJ/mol)
	Xllnty	T (°C)							
9MarF	19.74	1084	2cpx + pl + mt + il + fl		75.23	68.63	63.00		−1207
9MarG	30.02	1076	2cpx + pl + mt + il + fl		73.64	66.86	61.62		−1212
9MarH	38.39	1067	opx + cpx + pl + mt + il + fl		71.30		58.59	68.82	−1216
9MarD	49.37	1053	opx + cpx + pl + mt + il + fl		68.97		55.56	65.76	−1221
9MarJ	59.11	1036	opx + cpx + pl + mt + il + fl		65.81		52.53	62.57	−1227
9MarL	69.82	1012	2cpx + pl + mt + il + ap + fl		63.96	55.56	48.48		−1233
9MarM	79.99	970	2cpx + pl + mt + il + ap + fl		60.36	50.87	44.33		−1241
MCS Run	**Hybrid Lavas**		**Phases Present in Hybrid Lavas**	**Fo (ol)**	**Mg (cpx1)**	**Mg (cpx2)**	**An (pl)**	**Mg (opx)**	ΔfH^0_{hyb} (kJ/mol)
	Xllnty	T (°C)							
9MarF	6.44	1107.84	ol + cpx + pl + fl	73.00	77.98		67.68		−3010
9MarG	11.44	1100.36	ol + cpx + pl + fl	71.72	77.06		66.00		−3017
9MarH	16.74	1095.93	ol + 2cpx + pl + mt + il + fl	70.71	76.36	70.83	65.66		−3029
9MarD	24.53	1091.53	ol + 2cpx + pl + mt + il + fl	69.00	76.15	69.64	65.00		−3031
9MarJ	31.51	1086.28	2cpx + pl + mt + il + fl		74.55	68.45	64.00		−3039
9MarL	39.61	1079.43	2cpx + pl + mt + il + fl		73.64	67.26	62.63		−3048
9MarM	49.29	1068.24	opx + cpx + pl + mt + il + fl		70.69		60.00	68.28	−3061

(intermediate gray circles, ~Fo_{72}), which are interpreted to be in equilibrium with the hybrid magma, can be recreated in our lower-crystallinity (φ = 20–30) MCS models (Fig. 7). Both opx and low-Ca cpx compositions produced in the Fissure F mixing models (squares) have lower Mg# than measured pyroxenes from hybrid Episode 54 lavas (gray circles; Thornber *et al.*, 2003a), and we address these compositional disparities later in this section. MCS-produced pl compositions overlap with measured Fissure F pl compositions (gray circles) when the low-MgO endmember in our MCS models is 30–70% crystalline (Fig. 6); however, geothermometry estimates of crystallization *T* (Thornber *et al.*, 2003a) for pl present in Fissure F lavas are again higher than those produced in our MCS models (Fig. 7), likely reflecting the same caveats that we discussed above for the Fissure A–E models. Although Fe–Ti oxides are not present in Episode 54 lavas, they appear as hybrid phases in our MCS models, increasing from <2 vol % when the low-MgO endmember is 40% crystalline to ~16 vol % at the maximum modeled crystallinity (φ = 80). As myriad factors contribute to the saturation of a phase in rhyolite-MELTS, we consider the minor amounts (<2 vol %) of oxides to most likely reflect model uncertainties.

As with Fissure A–E lavas, we place additional constraints upon the thermodynamic state of the rift-stored magma body tapped to produce Fissure F lavas by comparing the compositions of modeled phases in equilibrium with the Fissure F low-MgO endmember to measured antecryst compositions in the erupted lavas (lightest gray circles). Equilibrium crystallization of the low-MgO endmember produces a mineral assemblage of

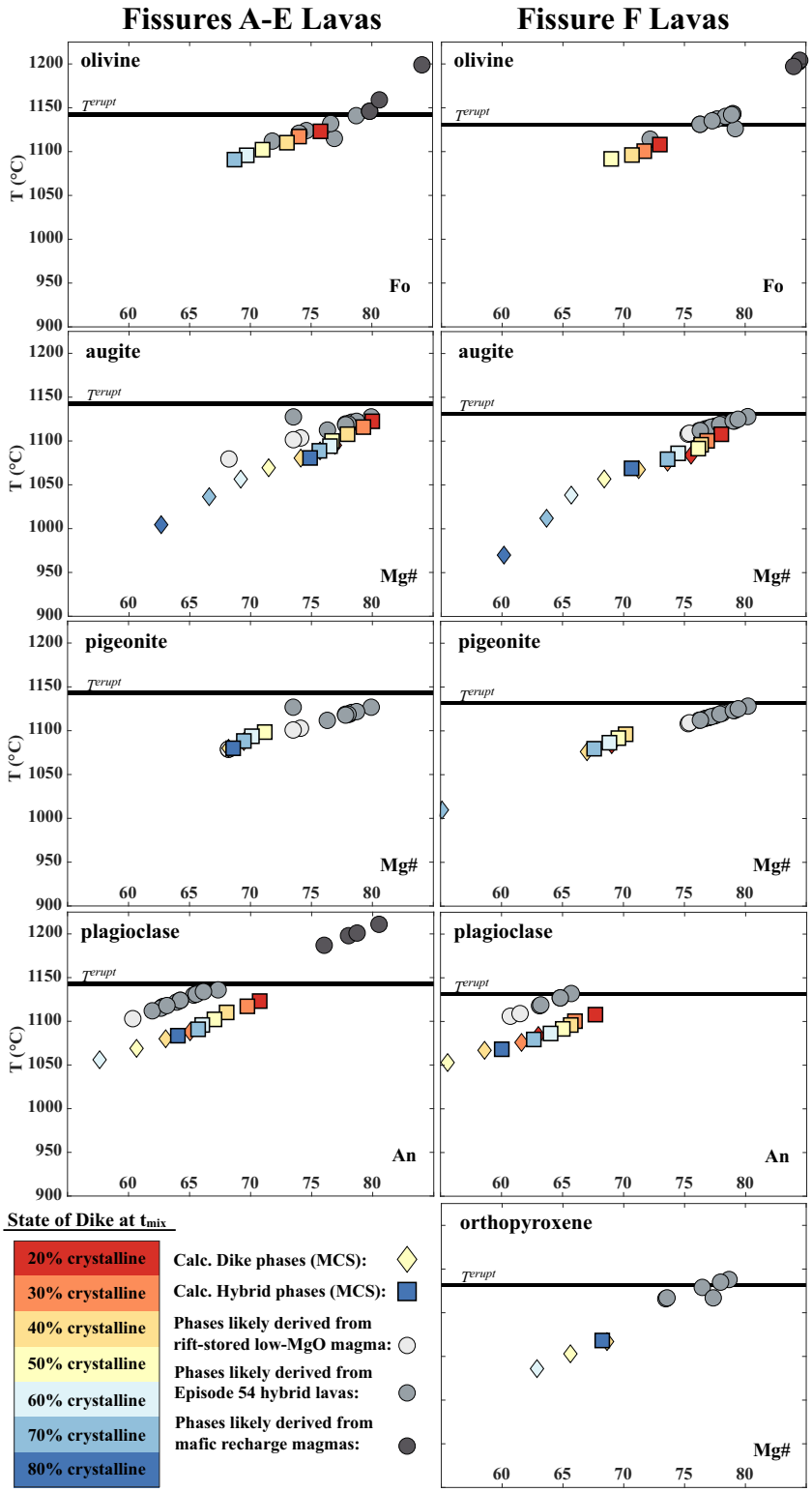

Fig. 7. Mineral compositions and crystallization temperatures of phases recovered from Episode 54 lavas as reported by Thornber *et al.* (2003a) compared against phases produced by Magma Chamber Simulator (MCS) mixing models. MCS-produced phases present in modeled hybrid lavas are represented by squares; diamonds represent calculated phases of the low-MgO (dike) magma immediately before hybridization. Symbol colors for MCS-produced phases represent the crystallinity of the modeled low-MgO magma at the time of recharge and hybridization. Minerals recovered from Episode 54 lavas are colored in greyscale according to their likely source, as classified by Thornber *et al.*, (2003a): light gray circles are mineral compositions likely derived from the low-MgO magma body; dark gray circles are mineral compositions likely derived from high-MgO mafic recharge magmas, and medium-gray circles are mineral compositions likely derived from Episode 54 hybrid lavas. Pyroxene Mg# is calculated as: 100 x $[Mg^{2+}/(Mg + Fe^{2+})]$ (Rollinson, 2014).

Table 7: Calculated bulk magma densities for hypothetical felsic endmember compositions at individual state points (P = 0.1 kbar)

Felsic mixing endmember for Fissures A-E (~23% fractionated from initial intrusion)			
Dike Crystallinity (%)	**φ assemblage**	**Dike T (°C)**	**ρ bulk magma (g/cm^3)**
19.64	ol + cpx + pl + mt + fl	1094	2.44
29.15	2cpx + pl + mt + il + fl	1088	2.37
39.42	2cpx + pl + mt + il + fl	1080	2.23
49.42	opx + cpx + pl + mt + il + fl	1069	2.09
58.83	opx + cpx + pl + mt + il + fl	1056	1.96
68.87	opx + cpx + pl + mt + il + fl	1036	1.84
78.99	opx + cpx + pl + mt + il + whit + fl	1004	1.71
Felsic mixing endmember for Fissure F (~35% fractionated from initial intrusion)			
Dike Crystallinity (%)	**φ assemblage**	**Dike T (°C)**	**ρ bulk magma (g/cm ^{3})**
19.74	2cpx + pl + mt + il + fl	1084	2.22
30.02	2cpx + pl + mt + il + fl	1076	2.06
38.39	opx + cpx + pl + mt + il + fl	1067	1.94
49.37	opx + cpx + pl + mt + il + fl	1053	1.79
59.11	opx + cpx + pl + mt + il + fl	1036	1.67
69.82	2cpx + pl + mt + il + fl	1012	1.56
79.99	2cpx + pl + mt + il + fl	970	1.48

augite + pigeonite + pl at T ≥ 1076°C (corresponding with φ ≤ 30); at T = 1067–1036°C (φ = 40–60), pigeonite is replaced by opx, but returns at T ≤ 1012°C (φ ≥ 70). Opx lamellae are present within some Fissure F cpx crystals, and a lone opx xenocryst was reported in Fissure F lavas by Thornber *et al.* (2003a). Although none of the forward models produce either opx or pigeonite with high Mg# comparable to those present in measured lavas (gray circles), the forward models *do* produce opx as an equilibrium hybrid phase when the low-MgO endmember is ~80% crystalline (Fig. 7). More likely, however, is that the observed orthopyroxene originates from the low-MgO magma, as orthopyroxene is a stable phase in the modeled low-MgO endmember over a range of T = 1067–1036°C, corresponding to φ = 40–60% (Fig. 7). Our best estimate of the state of the low-MgO endmember required to reproduce F^{avg} at the time of mixing is, therefore, φ ≈ 40, where opx is a stable phase in the low-MgO endmember at the time of mixing, and the observed common mineral assemblage of ol + cpx + pl is stable in modeled hybrid lavas.

The differences in the low-MgO endmembers for the Fissures A–E and Fissure F lavas may reflect the geometry of the eruption and differences in magma density. Fissure F is ~2.25 km up-rift of Fissure E, and at a higher elevation (~53 m elevation difference; see Fig. 1 & Sherrod *et al.*, 2021). Calculated bulk rock densities (Table 7) of the hypothetical low-MgO endmember compositions show that, at P = 0.1 kbar, the Fissure F low-MgO endmember magma (~35% fractionated from the original dike composition) is more buoyant than the less-evolved Fissure A–E low-MgO endmember (~23% fractionated), regardless of magma crystallinity. This is consistent with the Fissures A–E and Fissure F low-MgO endmembers being derived from a compositionally stratified, differentiating arrested dike. Fissure eruptions from feeder dikes have been shown to propagate laterally as an eruption progresses (Geshi *et al.*, 2020); lateral propagation of mafic recharge magmas interacting with an already emplaced, compositionally zoned and partially crystalline dike to form the final intrusive volume may explain why the final fissure of the eruptive sequence opened up-rift, and why its lavas were more evolved than the lavas erupted down-rift from Fissures A-E.

Linking petrology with geodesy—An integrated hypothesis for episode 54

A key goal of this study was to determine if a relationship can be established between syn-eruptive geodetic measurements and the geochemistry of lavas associated with the observed deformation. The timing, volume, location, and degree/direction of ground deformation for Kīlauea's Episode 54 eruption is well documented (Harris *et al.*, 1997; Owen *et al.*, 2000; Desmarais & Segall, 2007). The detailed eruption narrative of Episode 54, when paired with updated geodetic constraints and a detailed geochemical and petrological time-series of samples, affords a useful opportunity to link the eruption chronology and geochemical compositions to magma volumes estimated by two distinct methods, petrologic modeling and geodesy.

A revised volume estimate of the rift-stored low-MgO magma body

The results of our petrologic mixing models suggest that Episode 54 lavas erupted from Fissures A-E are a mixture of 57% rift-stored intrusion and 43% residential mafic magmas, and also that Episode 54 lavas erupted from Fissure F are a mixture of 60% rift-stored intrusion and 40% residential mafic magmas. Adopting the same method as Thornber *et al.* (2003a)—that ~60% of the 0.3 Mm^3 of erupted lavas are low-MgO component—we find the minimum volume of the rift-stored, multiply-saturated 1968 intrusion to be ~0.18 Mm^3. However, early Episode 55 lavas erupted before 1 August 1997 contain a number and variety of antecrysts derived from this low-MgO magma body, so this is an absolute minimum, and the true volume estimate must be greater than ~0.18 Mm^3.

Our calculated volume for the unknown fourth component referred to by Owen *et al.* (2000) is 7.51 Mm^3, but solely using a geodetic approach precludes identification of a magma composition (Segall, 2019). The 'missing' 7.51 Mm^3 could represent the volume of the underlying ERZ conduit, or it could be the volume of a single low-MgO endmember magma body involved in the Episode 54 mixing event, or it may represent any number of unerupted intrusions stored beneath the rift zone (Walker, 1986;

Garcia et al., 2000; Thornber et al., 2003a; Walker et al., 2019). Following the method of Thornber et al. (2003a) and using their same recharge rate of 0.3 Mm^3/day for the few weeks following Episode 54, if Thornber et al.'s proposed volume of 7.3 Mm^3 *was* indeed the ERZ conduit volume underlying Nāpau Crater, our volume closure estimate for the crystalline and evolved low-MgO magma body would be ~0.21 Mm^3—a volume just slightly larger than indicated by our petrologic mixing models. This may seem a reasonable result, but it does not account for the necessary volumes of low-MgO magma that were erupted during early Episode 55 (Table 3; Supp. Item E). Bulk major oxide compositions and disequilibrium antecrysts within lavas erupted from Pu'u'ō'ō'between 28 March 1997 and 1 August 1997 contain variable proportions of the Episode 54 low-MgO component (Fig. 2; see also Thornber et al., 2003a and 2003b), indicating that mafic recharge magmas flushed out any remaining rift-stored low-MgO magmas (Thornber et al., 2003a; Helz et al., 2014) during this five-month period. Further, a *drastic* drop in the proportion of low-MgO component in erupted lavas occurred after 1 August 1997, when transient movement (i.e. opening) of the rift zone ended (Fig. 3; see also Supp. Item E), implying that additional amounts of the low-MgO magma body continued to be incorporated into erupted lavas *until rift expansion ceased*. We, therefore, reason that the 7.51-Mm^3 of magma does, in fact, represent the volume of the low-MgO magma body involved in the Episode 54 mixing event (and subsequent recovery), and not the volume of the underlying ERZ conduit as proffered by Thornber et al. (2003a).

Reconciling geodetically determined intrusion volumes with petrologic modeling results

Our phase equilibria-guided model results are inconsistent with our volume closure calculations based on the geodetic data. Our volume closure calculations based on the point-source 'Mogi-style' models by Owen et al., (2000) and Segall et al., (2001), indicate that 15.4 Mm^3 of mafic magma mixed with a maximum of 7.51 Mm^3 of low-MgO, rift-stored magma body, yielding a mixing ratio of m^{mafic}:$m^{low\text{-}MgO} \approx 2$, in contrast to the predicted ratios of m^{mafic}:$m^{low\text{-}MgO} \approx 0.67$ to 0.75 as determined by our geochemical mixing models.

Geochemical trends make the different parageneses between erupted lavas quite apparent (Figs. 5-6); these results are consistent with the different eruption locations for Fissures A–E and Fissure F and underscore the complexity of the dike/rift system at Kilauea. MCS models suggest that lavas erupted from Fissures A–E formed as a mixture between a near-liquidus mafic magma derived from multiple sources within the Kīlauea edifice (MME, Table 5), and a variably fractionated and compositionally stratified arrested dike that erupted from fissure openings in Nāpau Crater. AE^{avg} (Table 4; Thornber et al., 2003a) is a mixture of 57% low-MgO magma ($f_{low\text{-}MgO} = 0.57 \pm 0.01$)—derived by ~23% fractionation (Table 5) of an initial composition similar to N68–4 (Tables 4-5; Jackson et al., 1975)—and 43% mafic magmas (MME, Table 5) derived from multiple sources within the Kīlauea edifice (m^{mafic}:$m^{low\text{-}MgO} \approx 0.75$; Table 5). The MCS models also suggest that the mafic magma interacted and mixed with a more evolved part of the same arrested dike to produce Fissure F lavas, but with a slightly greater mixing proportion of the low-MgO endmember. F^{avg} (Table 4; Thornber et al., 2003a) can be matched by a mixture of 60% low-MgO magma ($f_{low\text{-}MgO} = 0.60 \pm 0.005$)—derived by ~35% fractionation (m^{mafic}:$m^{low\text{-}MgO} \approx 0.67$; Table 5) of an initial composition similar to N68–4 (Tables 4-5; Jackson et al., 1975)—and 43% mafic magmas (MME, Table 5).

The transient accumulation of magmas and further mixing that occurred between the end of Episode 54 and the onset of steady-state activity at Kīlauea record post-eruptive mixing with and digestion of the rift-stored magma body as the plumbing system refilled. Episode 54 xenocrysts continued to be present in erupted Pu'u'ō'ō'lavas as the intrusion continued to grow (Fig. 2-3), before steady-state conditions were reestablished. Indeed, for magma batches to mix and homogenize to completion within a 22-hour period (Harris et al., 1997) would be unexpected. But, it is also unexpected that xenocrysts from the low-MgO magma would survive for months in an increasingly hotter, more mafic system (Thornber & Huebner, 1985), as would be required if the low-MgO rift-stored magma was completely digested by recharge magmas at the onset of the Episode 54 eruption. Hence, mixing with the rift-stored low-MgO magma *must* have continued to occur during post-eruptive intrusion growth.

We interpret the differences between the geodetic and petrologic model results as providing insight into how localized mixing events are documented in the rock record and highlighting how magma mixing is more often than not a heterogeneous process. Geodetic models—like those constructed by Owen et al. (2000) and Desmarais & Segall (2007)—may better describe the *entire* magma body, or what relative sources, proportions and volumes of magma may be involved. Geodetic studies may also account for any post-eruptive magma volume, recording events for the large-scale system that may not be captured in the chemistry of erupted lavas. The results of this study demonstrate that geochemical results can be instructive for identifying magma sources, magmatic processes, and timescales over which they happen, but they may only reflect a small portion of the magma body (White et al., 2006). Finally, because small-scale complexities unable to be resolved through geodetic models provide important insight to magmatic processes as well, a marriage of both techniques to evaluate magmatic processes is ideal.

CONCLUSIONS AND IMPLICATIONS

The April 2018 conclusion of Kīlauea's ~35 year-long Pu'u'ō'ō'eruption presents an opportunity for holistic, retrospective studies. After initial eruption onset, activity was characterized by periods of steady-state effusion, interrupted sporadically by intrusions into weakened areas of the ERZ (Thornber et al., 2015; Walker et al., 2019), sometimes resulting in brief fissure eruptions that produced low-MgO lavas choked with glomerocrystic crystal clots derived from more evolved, rift-stored magma bodies (Orr et al., 2015; Thornber et al., 2015). With each new intrusion, the underground storage and transport system of Kīlauea changed (Thornber, 2001; Thornber et al., 2003a; Orr, 2014; Orr et al., 2015; Lynn & Swanson, 2022). The results of our study demonstrate that whole rock and mineral chemistries coupled with thermodynamically constrained geochemical modeling, can provide new insight into mixing processes, the identity and physical state of rift stored bodies during mixing events, and the relative mixing proportions of mafic and rift-stored magmas that combine to erupt hybrid (*sensu lato*) lavas. This is particularly useful considering the relatively recent discovery of higher-silica evolved melts and mushes linked to more explosive activity (Rooyakkers et al., 2021; Weiser et al., 2022) at volcanoes that notably erupt effusively. A magma's explosivity is controlled by a number of factors, the most notable of which are temperature, initial crystal content, and dissolved volatile content (La Spina et al., 2021; Popa et al., 2021). Hence, identifying unerupted intrusive bodies in shallow volcanic edifices and understanding

their evolution and storage histories may provide insight on this newly emerging volcanic hazard.

Lavas erupted from Episode 54 fissures are basaltic and relatively aphyric, containing <5% phenocrysts and glomerocrystic clots of cpx + pl (Thornber *et al.*, 2003a), and have much lower MgO contents than lavas erupted before 30 January 1997 (Fig. 2). In agreement with previous research (Garcia *et al.*, 2000; Thornber *et al.*, 2003a), we conclude that a previously emplaced, evolved intrusion below Nāpau Crater mixed with mafic magmas from Kīlauea summit, Makaopuhi Crater and mafic drainback from the Pu'u'ō'ō'reservoir, to form the low-MgO basalts erupted during Episode 54. Our findings differ from those of Garcia *et al.* (2000) and Thornber *et al.* (2003a) in that we find that magmas derived from a single, compositionally stratified magma body that was intruded into Nāpau Crater in 1968 (N68-4; Jackson *et al.*, 1975) can mix with mafic Kīlauea magmas to reproduce average Episode 54 bulk lava, mineralogy and mineral compositions, without necessitating the interaction of multiple, low-MgO rift-stored magma bodies to produce Episode 54 lava compositions. Further, by constructing phase equilibria-based mixing models of Episode 54, we can better define the pre-eruptive state of the magmatic system. In contrast to the suggestion that the low-MgO intrusions were pure liquids at the time of mixing (Walker *et al.*, 2019), we find that the portion of the intrusion-derived magma needed to produce lavas erupted from Fissures A-E was ~23% fractionated from the initial bulk composition, and likely 40% to 50% crystalline at the time of mixing. We also conclude that a stratigraphically higher (and more evolved) region of the remnant 1968 intrusion located underneath the western edge of Nāpau Crater and sampled by the Fissure F eruptions, was produced by ~35% fractionation of the initial intrusion, and was likely 40% to 50% crystalline at the time of eruption. These results are inconsistent with the hypothesis of Walker *et al.* (2019) that the Fissure F lavas represent an unmixed low-MgO endmember composition. The mafic component mixed with the two, now compositionally distinct but petrogenetically related, low-MgO endmembers in proportions of $m^{mafic}:m^{low\text{-}MgO} \approx 0.75$ and $m^{mafic}:m^{low\text{-}MgO} \approx 0.67$ to produce Fissures A–E and Fissure F lavas, respectively. We also find that the proportions of the individual magma sources, as constrained by geodetic measurements, can be used as a guide to construct mixing endmembers, but directly linking geodetic volume estimates to magma chemistry is complicated by complex mixing processes that occur rapidly prior to eruption, and a direct link between the total volume of a magma body and its geochemistry is likely complicated by incomplete mixing that occurs over short distances and timescales. This novel application of the Magma Chamber Simulator could be widely employed at other volcanic systems where the conditions of a partially crystalline magma are in question and may prove useful for future studies of volcanic hazards.

Conflict of Interest Statement

The authors declare that they have no known competing financial interests or personal relationships that could have appeared to influence the work reported in this paper.

SUPPLEMENTARY DATA

Supplementary data are available at Journal of Petrology online.

AUTHOR CONTRIBUTIONS

This project was conceptualized by Wendy Bohrson and Frank Spera, and designed by Melissa Scruggs and Frank Spera. Model refinement, investigation of the research question, and formal analysis of model results was conducted by Melissa Scruggs, with supervising contributions and guidance from Frank Spera, Matt Rioux, and Roberta Rudnick. This manuscript was written by Melissa Scruggs, with revisions and edits from Frank Spera, Matt Rioux, and Wendy Bohrson; visualization and curation of data produced by this study was conducted and maintained by Melissa Scruggs.

FUNDING

We wish to thank the National Science Foundation for funding development of the Magma Chamber Simulator. This study was funded in part by National Science Foundation Grants NSF-1551052 and NSF-0440010 to WAB, and NSF-2151039 to FJS.

ACKNOWLEDGEMENTS

We would like to thank Roberta Rudnick for her invaluable guidance and insight on many aspects of this project, in addition to Carl Thornber and Michael Garcia for their discussions and communications regarding the nature of this particular eruptive episode. Finally, we would like to thank Kendra J. Lynn and an anonymous reviewer, whose comments greatly improved the strength and clarity of this manuscript.

DATA AVAILABILITY

This study does not contain any new geochemical data or present any new software code. Geochemical compositions examined in this study were obtained from Thornber (2001) and Thornber *et al.* (2003a, 2003b). MCS data underlying this article are available in the online supplementary material.

REFERENCES

Bohrson, W. A., Spera, F. J., Ghiorso, M. S., Brown, G. A., Creamer, J. B. & Mayfield, A. (2014). Thermodynamic model for energy-constrained open-system evolution of crustal magma bodies undergoing simultaneous recharge, assimilation, and crystallization: the Magma Chamber Simulator. *Journal of Petrology* **55**(9), 1685–1717. https://doi.org/10.1093/petrology/egu036.

Bohrson, W. A., Spera, F. J., Heinonen, J. S., Brown, G. A., Scruggs, M. A., Adams, J. V., Zeff, G. & Suikkanen, E. (2020). Diagnosing open-system magmatic processes using the Magma Chamber Simulator (MCS): part I—major elements and phase equilibria. *Contributions to Mineralogy and Petrology* **175**, 104. https://doi.org/10.1007/s00410-020-01722-z.

Clague, D. A. & Sherrod, D. R. (2014) Growth and degradation of Hawaiian volcanoes. In: Poland M. P., Taeko J. T. & Landowski C. M. (eds) *Characteristics of Hawaiian Volcanoes*. U.S. Geological Survey Professional Paper 1801, pp.97–148.

Desmarais, E. K. & Segall, P. (2007). Transient deformation following the 30 January 1997 dike intrusion at Kīlauea Volcano, Hawai'i. *Bulletin of Volcanology* **69**, 353–363. https://doi.org/10.1007/s00445-006-0080-7.

Edmonds, M., Sides, I. & Maclennan, J. (2015) *Insights into mixing, fractionation, and degassing of primitive melts at Kīlauea Volcano, Hawai'i*. In: Heliker C., Swanson D. A. & Takahashi T. J. (eds) *The Pu'u'ō'ō'-Kupaianaha Eruption of Kīlauea Volcano, Hawai'i: The First 20 Years*. U.S. Geological Survey Professional Paper 1676, pp.323–350.

von Engelhardt, W. (1989). Remarks on "ratio plots" and "mixing lines". *Geochimica et Cosmochimica Acta* **53**, 2443–2444. https://doi.org/10.1016/0016-7037(89)90364-5.

Gansecki, C., Lee, R. L., Shea, T., Lundblad, S. P., Hon, K. & Parcheta, C. (2019). The tangled tale of Kīlauea's 2018 eruption as told by geochemical modeling. *Science* **366**, eaaz0147. https://doi.org/10.1126/science.aaz0147.

Garcia, M. O. (2003). A Petrologic Perspective of Kilauea Volcano's Summit Magma Reservoir. *Journal of Petrology*, **44**(12), 2313-2339. https://doi.org/10.1093/petrology/egg079.

Garcia, M. O., Rhodes, J. M., Wolfe, E. W., Ulrich, G. E. & Ho, R. A. (1992). Petrology of lavas from episodes 2-47 of the Puu Oo eruption of Kīlauea Volcano, Hawai'i: evaluation of magmatic processes. *Bulletin of Volcanology* **55**, 1–16. https://doi.org/10.1007/BF00301115.

Garcia, M. O., Pietruszka, A. J., Rhodes, J. M. & Swanson, K. (2000). Magmatic processes during the prolonged Pu'u'ō'ō' eruption of Kīlauea Volcano, Hawai'i. *Journal of Petrology* **41**(7), 967–990. https://doi.org/10.1093/petrology/41.7.967.

Geshi, N., Browning, J. & Kusumoto, S. (2020). Magmatic overpressures, volatile exsolution and potential explosivity inferred via dike aspect ratios. *Nature Scientific Reports* **10**(9406). https://doi.org/10.1038/s41598-020-66226-z.

Ghiorso, M. S. & Gualda, G. A. R. (2015). An H_2O-CO_2 mixed fluid saturation model compatible with rhyolite-MELTS. *Contributions to Mineralogy & Petrology* **169**(53). https://doi.org/10.1007/s00410-015-1141-8.

Gualda, G. A. R., Ghiorso, M. S., Lemons, R. V. & Carley, T. L. (2012). Rhyolite-MELTS: a modified calibration of MELTS optimized for silica-rich, fluid-bearing magmatic systems. *Journal of Petrology* **53**(5), 875–890. https://doi.org/10.1093/petrology/egr080.

Harris, A. J. L., Keszthelyi, L., Flynn, L. P., Mouginis-Mark, P. J., Thornber, C., Kauahikaua, J., Sherrod, D., Trusdell, F., Sawyer, M. W. & Flament, P. (1997). Chronology of the episode 54 eruption at Kīlauea volcano, Hawai'i, from GOES-9 satellite data. *Geophysical Research Letters* **24**(24), 3281–3284. https://doi.org/10.1029/97GL03165.

Helz, R. T., Clague, D. A., Sisson, T. W. & Thornber, C. R. (2014) Petrologic insights into basaltic volcanism at historically active Hawaiian volcanoes. In: Poland M. P., Taeko J. T. & Landowski C. M. (eds) *Characteristics of Hawaiian Volcanoes*. U.S. Geological Survey Professional Paper 1801, pp.237–292.

Holland, T. J. B. & Powell, R. (1998). An internally consistent thermodynamic data set for phases of petrological interest. *Journal of Metamorphic Geology* **16**, 309–343. https://doi.org/10.1111/j.1525-1314.1998.00140.x.

Jackson, D. B., Swanson, D. A., Koyanagi, R. Y. & Wright, T. L. (1975) *The August and October 1968 East Rift Eruptions of Kīlauea Volcano, Hawai'i*. U.S. Geological Survey Professional Paper 890, pp.1–33.

La Spina, G., Arzilli, F., Llewellin, E. W., Burton, M. R., Clarke, A. B., de'Michieli Vitturi, M., Polacci, M., Hartley, M. E., Di Genova, D. & Mader, H. M. (2021). Explosivity of basaltic lava fountains is controlled by magma rheology, ascent rate and outgassing. *Earth & Planetary Science Letters* **553**, 116658. https://doi.org/10.1016/j.epsl.2020.116658.

Langmuir, C. H., Vocke, R. D., Jr., Hanson, G. N. & Hart, S. R. (1978). A general mixing equation with applications to Icelandic basalts. *Earth and Planetary Science Letters* **37**, 380–392. https://doi.org/10.1016/0012-821X(78)90053-5.

Lynn, K. J. & Swanson, D. A. (2022). Olivine and glass chemistry record cycles of plumbing system recovery after summit collapse events at Kīlauea Volcano, Hawa'i. *Journal of Volcanology and Geothermal Research* **426**, 107540. https://doi.org/10.1016/j.jvolgeores.2022.107540.

Mangan, M.T., Cashman, K.V. & Swanson, D.A. (2014) The dynamics of Hawaiian-style eruptions: a century of study. In: Poland M.P., Taeko J.T. & Landowski C.M. (eds) *Characteristics of Hawaiian Volcanoes. U.S. Geological Survey Professional Paper* **1801**, pp. 323–354.

Moore, J. G. & Koyanagi, R. Y. (1969). The October 1963 eruption of Kīlauea volcano Hawai'i. *U.S. Geological Survey Professional Paper* **614-C**, 13 p.

Neal, C. A., Brantley, S. R., Antolik, L., Babb, J. L., Burgess, M., Calles, K., Cappos, M., Chang, J. C., Conway, S., Desmither, L., Dotray, P., Elias, T., Fukunaga, P., Fuke, S., Johanson, I. A., Kamibayashi, K., Kauahikaua, J., Lee, R. L., Pekalib, S., Miklius, A., Million, W., Moniz, C. J., Nadeau, P. A., Okubo, P., Parcheta, C., Patrick, M. R., Shiro, B., Swanson, D. A., Tollett, W., Trusdell, F., Younger, E. F., Zoeller, M. H., Montgomery-Brown, E. K., Anderson, K. R., Poland, M. P., Ball, J. L., Bard, J., Coombs, M., Dietterich, H. R., Kern, C., Thelen, W. A., Cervelli, P. F., Orr, T., Houghton, B. F., Gansecki, C., Hazlett, R., Lundgren, P., Diefenbach, A. K., Lerner, A. H., Waite, G., Kelley, P., Clor, L., Werner, C., Mulliken, K., Fisher, G. & Damby, D. (2019). The 2018 rift eruption and summit collapse of Kīlauea Volcano. *Science* **363**, 367–374. https://doi.org/10.1126/science.aav7046.

Orr, T.R. (2014). The June–July 2007 collapse and refilling of the Pu'u'ō'ō' Crater, Kīlauea Volcano, Hawai'i: U.S. Geological Survey Scientific Investigations Report 2014–5124, 15 p. doi:https://doi.org/10.3133/sir20145124.

Orr, T. R., Poland, M. P., Patrick, M. R., Thelen, W. A., Sutton, A. J., Elias, T., Thornber, C. R., Parcheta, C. & Wooten, K. M. (2015) *Kīlauea's 5-9 March 2011 Kamoamoa Fissure Eruption and its relation to 30+ years of activity* from Pu'u'ō'ō'. In: Carey R., Cayol V., Poland M. & Weis D. (eds) *Hawaiian Volcanoes: From Source to Surface*. Hoboken, NJ: John Wiley & Sons, pp.393–420.

Owen, S., Segall, P., Lisowski, M., Miklius, A., Murray, M., Bevis, M. & Foster, J. (2000). January 30, 1997 eruptive event on Kīlauea Volcano, Hawai'i, as monitored by continuous GPS. *Geophysical Research Letters* **27**(17), 2757–2760. https://doi.org/10.1029/1999GL008454.

Popa, R., Bachmann, O. & Huber, C. (2021). Explosive or effusive style of volcanic eruption determined by magma storage conditions. *Nature Geoscience* **14**, 781–786. https://doi.org/10.1038/s41561-021-00827-9.

Putirka, K. (2016). Rates and styles of planetary cooling on Earth, Moon, Mars, and Vesta, using new models for oxygen fugacity, ferric-ferrous ratios, olivine-liquid Fe-Mg exchange, and mantle potential temperature. *American Mineralogist* **101**, 819–840. https://doi.org/10.2138/am-2016-5402.

Rhodes, J. M. (1995) The 1852 and 1868 Mauna Loa picrite eruptions: clues to parental magma compositions and the magmatic plumbing system. In: Rhodes J. M. & Lockwood J. P. (eds) *Mauna Loa Revealed: structure, composition, history, and hazards*Geophysical Monograph Series vol. 92. American Geophysical Union, pp.241–262.

Rollinson, H. R. (2014) *Using Geochemical Data: Evaluation, Presentation, Interpretation*. Longman Group UK Ltd, Essex, p.384.

Rooyakker, S. M., Stix, J., Berlo, K., Petrelli, M. & Sigmundsson, F. (2021). Eruption risks from covert silicic magma bodies. *Geology* **49**(8), 921–925. https://doi.org/10.1130/G48697.1.

Segall, P. (2019). Magma chambers: what we can, and cannot, learn from volcano geodesy. *Philosophical Transactions of the Royal Society A* **377**, 20180158. https://doi.org/10.1098/rsta.2018.0158.

Segall, P., Cervelli, P., Owen, S., Lisowski, M. & Miklius, A. (2001). Constraints on dike propagation from continuous GPS

measurements. *Journal of Geophysical Research* **106**(B9), 19301–19317. https://doi.org/10.1029/2001JB000229.

Sherrod, D.R., Sinton, J.M., Watkins, S.E., and Brunt, K.M. (2021), Geologic map of the State of Hawai'i: U.S. Geological Survey Scientific Investigations Map 3143, pamphlet 72 p., 5 sheets, scales 1:100,000 and 1:250,000, doi:https://doi.org/10.3133/sim3143.

Sutton, A. J., Elias, T. & Kauahikaua, J. (2003) Lava-effusion rates for the Pu'u'ō'ō'-Kupaianaha eruption derived from SO_2 emissions and very low frequency (VLF) measurements. In: Heliker C., Swanson D. A. & Takahashi T. J. (eds) *The Pu'u'ō'ō'-Kupaianaha Eruption of Kīlauea Volcano, Hawai'i: The First 20 Years*. U.S. Geological Survey Professional Paper 1676, pp.137–148.

Thornber, C. R. (2001). Olivine-liquid relations of lava erupted by Kīlauea Volcano from 1994 to 1998: Implications for shallow magmatic processes associated with the ongoing East-Rift-Zone eruption. *The Canadian Mineralogist* **39**, 239–266. https://doi.org/10.2113/gscanmin.39.2.239.

Thornber, C. R. & Huebner, J. S. (1985). Dissolution of olivine in basaltic liquids: experimental observations and applications. *American Mineralogist* **70**, 934–945.

Thornber, C. R., Sherrod, D., Heliker, C., Kauahikaua, J., Trusdell, F., Lisowski, M. & Okubo, P. (1997). *Kilauea's ongoing eruption: Napau crater revisited after 14 years*, EOS, transactions. *American Geophysical Union* **78**, 329.

Thornber, C. R., Heliker, C., Sherrod, D. R., Kauahikaua, J. P., Miklius, A., Okubo, P. G., Trusdell, F. A., Budahn, J. R., Ridley, W. I. & Meeker, G. P. (2003a). Kīlauea East Rift Zone magmatism: an episode 54 perspective. *Journal of Petrology* **44**(9), 1525–1559. https://doi.org/10.1093/petrology/egg048.

Thornber, C. R., Hon, K., Heliker, C. & Sherrod, D. A. (2003b) *A compilation of whole-rock and glass major-element geochemistry of Kīlauea Volcano, Hawai'i, near-vent eruptive products: January 1983 through September 2001*. U.S. Geological Survey Open-File Report 03–477, p.8.

Thornber, C. R., Orr, T. R., Heliker, C. & Hoblitt, R. P. (2015) *Petrologic testament to changes in shallow magma storage and transport during 30+ years of recharge and eruption at Kīlauea Volcano, Hawai'i*. In: Carey R., Cayol V., Poland M. & Weis D. (eds) *Hawaiian Volcanoes: From Source to Surface*. Hoboken, NJ: John Wiley & Sons, pp.147–188.

Walker, G. P. L. (1986). Koolau Dike Complex, Oahu: intensity and origin of a sheeted-dike complex high in a Hawaiian volcanic edifice. *Geology* **14**, 310–313. https://doi.org/10.1130/0091-7613(1986)14<310:KDCOIA>2.0.CO;2.

Walker, B. H., Garcia, M. O. & Orr, T. R. (2019). Petrologic insights into rift zone magmatic interactions from the 2011 eruption of Kīlauea Volcano, Hawai'i. *Journal of Petrology* **60**(11), 2051–2075. https://doi.org/10.1093/petrology/egz064.

Wallace, P. J. & Anderson, A. T., Jr. (1998). Effects of eruption and lava drainback on the H_2O contents of basaltic magmas at Kīlauea Volcano. *Bulletin of Volcanology* **59**, 327–344. https://doi.org/10.1007/s004450050195.

Waters, L. E. & Lange, R. A. (2015). An updated calibration of the plagioclase-liquid hygrometer-thermometer applicable to basalts through rhyolites. *American Mineralogist* **100**, 2172–2184. https://doi.org/10.2138/am-2015-5232.

White, S. M., Crisp, J. A. & Spera, F. J. (2006). Long-term volumetric eruption rates and magma budgets. *Geochemistry Geophysics Geosystems* **7**(3), Q03010. https://doi.org/10.1029/2005GC001002.

Wieser, P. E., Edmonds, M., Gansecki, C., Maclennan, J., Jenner, F. E., Kunz, B., Antoshechkina, P., Trusdell, F., Lee, R. L. & EIMF (2022). Explosive activity on Kīlauea's Lower East Rift Zone fueled by a volatile-rich, dacitic melt. *Geochemistry, Geophysics, Geosystems* **23**(2), e2021GC010046. https://doi.org/10.1029/2021GC010046.

Wieser, P. E., Kent, A. J. R., Till, C. B., Donovan, J., Neave, D. A., Blatter, D. L. & Krawczynski, M. J. (2023). Barometers behaving badly I: assessing the influence of analytical and experimental uncertainty on clinopyroxene thermobarometry calculations at crustal conditions. *Journal of Petrology* **64**(2), egac126. https://doi.org/10.1093/petrology/egac126.

Wright, T. L. & Fiske, R. S. (1971). Origin of the differentiated and hybrid lavas of Kīlauea Volcano, Hawai'i. *Journal of Petrology* **12**(1), 1–65. https://doi.org/10.1093/petrology/12.1.1.

Wright, T. L. & Klein, F. W. (2014) *Two hundred years of magma transport and storage at Kīlauea Volcano, Hawai'i, 1790–2008*. U.S. Geological Survey Professional Paper 1806, 240 p.

Wright, T. L., Kinoshita, W. T. & Peck, D. L. (1968). March 1965 eruption of Kīlauea Volcano and the formation of Makaopuhi Lava Lake. *Journal of Geophysical Research* **73**(10), 3181–3205. https://doi.org/10.1029/JB073i010p03181.

Deltech Furnaces

Sustained operating temperatures to 1800° Celsius

www.deltechfurnaces.com

Gas Mixing System

An ISO 9001:2015 certified company

Custom Vertical Tube

ASME NQA-1 2008 Nuclear Quality Assurance

Standard Vertical Tube

Control systems are certified by Intertek UL508A compliant

Bottom Loading Vertical Tube